

Retrieval of aerosol properties from zenith sky radiance measurements

Sara Herrero-Anta¹, Roberto Román¹, David Mateos¹, Ramiro González¹, Juan Carlos Antuña-Sánchez², Marcos Herreras-Giralda², Antonio Fernando Almansa^{3,4}, Daniel González-Fernández¹, Celia Herrero del Barrio¹, Carlos Toledano¹, Victoria E. Cachorro¹ and Ángel M. de Frutos¹.

¹Group of Atmospheric Optics, University of Valladolid, Paseo de Belén 7, 47011 Valladolid, Spain.

²GRASP SAS, Remote Sensing Developments, Villeneuve D'Ascq, France

³Izaña Atmospheric Research Center (IARC), State Meteorological Agency of Spain (AEMET), 38001 Santa Cruz de Tenerife, Spain.

⁴Cimel Electronique, 75011 Paris, France.

Correspondence to: Sara Herrero-Anta (sara@goa.uva.es)

Abstract. This study explores the potential to retrieve aerosol properties with the GRASP algorithm (Generalized Retrieval of Atmosphere and Surface Properties) using as input measurements of zenith sky radiance (ZSR), which are sky radiances measured in the zenith direction, recorded at four wavelengths by a ZEN-R52 radiometer. To this end, the ZSR measured at 440, 500, 675 and 870 nm by a ZEN-R52 (ZSR_{ZEN}), installed in Valladolid (Spain), is employed. This instrument is calibrated intercomparing the signal of each channel with coincident ZSR values simulated (ZSR_{SIM}) at the same wavelengths with a radiative transfer model (RTM). These simulations are carried out using the GRASP forward module as RTM and the aerosol information from a collocated CE318 photometer belonging to the AERONET network (Aerosol and Robotic Network) as input. Dark signal and the signal dependence on temperature are characterized and included in the calibration process. The uncertainties on each channel are quantified by an intercomparison with a collocated CE318 photometer, obtaining lower values for shorter wavelengths; between 3% for 440 nm and 21% for 870 nm. The proposed inversion strategy for the aerosol retrieval using the ZSR_{ZEN} measurements as input, so-called GRASP-ZEN, assumes the aerosol as an external mixture of five pre-calculated aerosol types. A sensitivity analysis is conducted using synthetic ZSR_{ZEN} measurements, pointing out that these measurements are sensitive to aerosol load and type. It also assesses that the retrieved aerosol optical depth (AOD) values in general overestimates the reference ones by 0.03, 0.02, 0.02 and 0.01 for 440, 500, 675, 870 nm, respectively. The calibrated ZSR_{ZEN} measurements, recorded during two and half years at Valladolid, are inverted by GRASP-ZEN strategy to retrieve some aerosol properties like AOD. The retrieved AOD shows a high correlation with respect independent values obtained from ~~the~~ collocated AERONET CE318 photometer, with a determination coefficient (r^2) ~~about~~ ~~of~~ 0.86, 0.85, 0.79 and 0.72 for 440, 500, 675 and 870 nm, respectively, and finding uncertainties between 0.02 and 0.03 with respect to the AERONET values. ~~Finally, the retrieval~~ ~~Finally, it is studied the goodness~~ of other ~~retrieved~~ aerosol properties, like aerosol volume concentration for total, fine and coarse modes (VCT, VCF, VCC) is also explored. ~~The comparison against independent values from AERONET presents r^2 values of 0.57, 0.56 and 0.66, and uncertainties of 0.009, 0.016 and 0.02 $\mu\text{m}^3/\mu\text{m}^2$ for VCT, VCF, VCC respectively.~~

Keywords: zenith sky radiance, ZEN, GRASP, aerosol optical depth, AERONET, photometer

1. Introduction

Atmospheric aerosols constitute the biggest source of uncertainty in the assessment of Climate Change as assessed by Myhre et al., (2013), and yet, one decade later, ~~not significant improvements have been made on this respect this issue still remains~~ (Forster-Cissé et al., 20221). This is largely due to their high spatial and temporal variability across the globe and the complexity of its interaction with clouds (aerosol-cloud interactions) and solar radiation (aerosol-radiation interactions) (Boucher et al., 2013).

For a better understanding of aerosols and their behaviour and interactions, ~~it is needed~~ a high spatial and temporal monitoring coverage ~~is required~~. Satellite measurements provides, in general, a high spatial resolution covering the whole Earth, but with a low ~~temporal~~ ~~time~~ resolution. On the other hand, some global ground-based networks, like AERONET (Aerosol Robotic Network; Holben et al., 1998), were established to monitor aerosols around the globe. ~~In the case of AERONET, this network~~ counts with hundreds of stations distributed worldwide and imposes standardization of instruments, calibration,

51 processing and data distribution. The standard instrument of AERONET is CE318 photometer
52 manufactured by (Cimel Electronique SAS), which records measurements of sun (~~and also lunar in recent~~
53 ~~models or lunar, if available~~) irradiance and sky radiance in several wavelengths. Aerosol optical depth
54 (AOD) can be derived using sun (or lunar)the measurements, ~~of sun (or lunar if available)~~ such as in the
55 case of AERONET, applying the Beer-Lambert-Bouguer law on the instrument's output voltage as
56 described in Holben et al. (1998) and Giles et al. (2019). AERONET also employs an inversion algorithm
57 to retrieve ~~s more~~ complex aerosol properties, like aerosol size distribution and refractive indices. This
58 algorithm considers ~~using an inversion algorithm that uses as input sky-sky~~ radiances at different angles
59 and wavelengths, together along with the AOD, ~~values as input~~ (Sinyuk et al., 2020).

60 Another inversion algorithm is ~~the~~ GRASP ~~code~~ (Generalized Retrieval of Atmosphere and Surface
61 Properties; www.grasp-open.com), which is a free and open-source code that allows a flexible retrieval of
62 aerosol properties using measurements taken from many different instruments and a combination of them
63 (Dubovik et al., 2014; 2021). The continuous development and versatility of the code enable the
64 exploration allows to explore of new alternatives for its application alternatives to apply the code to
65 different instruments. In this ~~sense regard~~, some authors have utilized ~~used~~ GRASP to retrieve aerosol
66 properties using as input, among others, data from ~~as input measurements, among others, of~~ satellites (Chen
67 et al., 2020; Wei et al., 2021); nephelometers (Espinosa et al., 2017); multi-wavelength AOD (Torres et al.,
68 2017); AOD and sky radiance from photometers with signal from lidars (Lopatin et al., 2013; Benavent-
69 Oltra et al., 2017; Tsekeri et al., 2017; Molero et al., 2020) or ceilometers (Román et al., 2018; Titos et al.,
70 2019; Herreras et al., 2019); stand-alone all-sky cameras (Román et al., 2022), and their combination with
71 lunar photometers (Román et al., 2017) and lidar (Benavent-Oltra et al., 2019).

72 A new instrument that could be used for GRASP retrievals is the ZEN-R52, manufactured by (Sieltec
73 Canarias S.L.), which has already been used to retrieve AOD values by other methods (Almansa et al.,
74 2020). The ZEN-R52 measures ~~the~~ zenith sky radiances (ZSR) at five different wavelengths every minute,
75 giving continuous ZSR values during daytime at 440, 500, 675, 870 and 940 nm (this latter channel is
76 dedicated to the study retrieval of water vapour). As advantage, this instrument has not moving parts and,
77 in general, is cheaper than more complex photometers, which allows the installation of more instruments
78 obtaining a higher spatial coverage One advantage of this instrument is that it does not have moving parts
79 and is cheaper than more complex photometers. This affordability could enable the installation of multiple
80 instruments, thereby achieving a higher spatial coverage. Almansa et al., (2020) presented the ZEN-R52
81 and developed a method to retrieve AOD values from ZSR using a look-up table (LUT) created for the site
82 of study, Izaña (Canary Island, Spain), considering uniquely dust aerosol, which is the main aerosol ~~type~~
83 in the area due to the proximity to the Saharan desert.

84 In this framework, the main objective of ~~the~~ presents work is to develop a new methodology to retrieve
85 AOD and other aerosol properties with GRASP, using calibrated ZSR at 440, 500, 675 and 870 nm from a
86 ZEN-R52 instrument. This retrieval strategy is not linked to the place of study and therefore it allows to
87 distribute the instrument worldwide, avoiding the need to create a different LUT for each site. In addition,
88 we propose an in-situ method for the calibration of the ZEN-R52.

89 Following this Section 1, dedicated to the introduction, the ~~paper following paper~~ is structured
90 organized as follows. Section 2 gathers information regarding the instrumentation and retrieval methods
91 employed, as well as a description of the ~~the~~ site study location. The procedure and results of the radiance
92 calibration of the ZSR at the four wavelengths used are explained in Section 3, ~~while~~ Section 4 is used
93 to evaluate and drive a sensitivity study of the algorithm employed for the retrieval of aerosol properties.
94 Finally, an analysis of the aerosol properties results obtained retrieved using the proposed newly developed
95 methodology for the retrieval of aerosol properties are ~~is~~ shown in Section 5, and Section 6 summarizes the
96 main conclusions of the study.

97 2. Data and method

98 2.1 Site and instrumentation

99 2.1.1 Valladolid GOA-UVa station

101 The place of study is located in Valladolid (Spain), a medium-sized city with a population of about 400000
102 inhabitants, including the metropolitan area. The city's climate is Mediterranean (Csb Köppen-Geiger
103 climate classification). It presents predominantly 'clean continental' aerosol with frequent episodes of

104 Saharan desert dust intrusions, especially in summer, when the highest AOD monthly mean values are
105 reached (Bennouna et al., 2013; Román et al., 2014; Cachorro et al., 2016).

106 The Group of Atmospheric Optics of the University of Valladolid (GOA-UVa) manages an
107 instrumentation platform installed on the rooftop of the Science Faculty (41.6636° N, 4.7058° W; 705 m
108 asl), where diverse remote sensing instruments continuously run providing complementary information
109 about radiance, clouds, water vapour, trace gases and aerosols. Two instruments from this station are used
110 in this work: the CE318 photometer and the ZEN-R52 radiometer. The corresponding calculations and
111 additional information will be referred and obtained for this location.

112 2.1.2 CE318 photometers and AERONET products

113 Since 2006 the GOA-UVa has been one of the calibration facilities in charge of the calibration of
114 AERONET standard instruments and is currently part of the European infrastructure ACTRIS (Aerosol,
115 Clouds and Trace Gases Research Infrastructure). The group is also actively contributing to the solar and
116 moon photometry research (Barreto et al., 2019; González et al., 2020; Román et al., 2020). Due to
117 calibration purposes, the GOA-UVa has ~~almost~~ always two reference AERONET photometers (masters)
118 continuously operating on its rooftop platform for the calibration of ~~the field~~ instruments by
119 intercomparison with these masters. The CE318 measures direct sun (and lunar for the recent model CE318-
120 T; Barreto et al., 2016) irradiance at several narrow spectral bands by means of a rotating filters wheel.
121 These direct measurements are used to derive the AOD (Giles et al., 2019) for all the available filters with
122 and uncertainty of ± 0.01 for wavelengths longer than 440 nm and ± 0.02 for the UV (Holben et al., 1998).
123 Sky radiances at several wavelengths are also measured by the CE318 on different scanning scenarios, and
124 these sky radiances are combined with AOD values in the AERONET inversion algorithm to obtain
125 microphysical and optical aerosol properties like aerosol volume size distribution and complex refractive
126 index (Sinyuk et al., 2020). The sky radiances are calibrated against a calibrated integrating sphere
127 following AERONET standards, obtaining an uncertainty of 5% ~~for those measurements~~ (Holben et al.,
128 1998).

129 In this work, we use AOD, sky radiance values and ~~retrieved inversion~~ aerosol products ~~from inversions~~
130 from AERONET version 3 level 1.5, ~~which is quality assured~~. These data ~~have been~~ can be directly
131 downloaded from the AERONET webpage (<https://aeronet.gsfc.nasa.gov>), which include near-real-time
132 automatic cloud-screening and quality control filters (level 1.5). The inversion products with a sky error
133 above ~~105%~~ have been rejected in this study to warranty the quality of the retrievals.

134 2.1.3 ZEN-R52

135 The main instrument used in this work is the ZEN-R52 radiometer, installed in the GOA-UVa
136 platform since April 2019. Since that moment the ZEN-R52 has been continuously operating in Valladolid,
137 except for some short malfunction periods caused by technical issues. This study uses the recorded data
138 from April 2019 until September 2021. The device was jointly developed by Sieltec Canarias S.L. and the
139 Izaña Atmospheric Research Center (IARC) to monitor AOD from sky radiance measurements at the zenith
140 direction and at different spectral bands (Almansa et al., 2017; 2020). The instrument has five filters with
141 nominal wavelengths centred at 440, 500, 675, 870 and 940 nm with a bandwidth of 10 nm and an estimated
142 precision of ± 2 nm in the central wavelength. Each filter is ~~placed~~ over a silicon diode (~~350–1050 nm~~) with
143 a 16-bit resolution, over a high dynamic acquisition range. The 940 nm filter was recently included in this
144 new version for precipitable water vapour retrieval, but this channel ~~will~~ is not ~~be~~ used in this work since ~~#~~
145 ~~is it~~ focus ~~esed on on~~ aerosols. The ZEN-R52 optical configuration achieves a field of view smaller than 2° .
146 It is equipped with a small aluminium weatherproof and protected by a thick borosilicate BK7 window,
147 with no moving parts. All ~~of of t~~ this is mounted in such a way that the collimated sky radiance in the
148 direction of the zenith reaches ~~to~~ the sensors. The instrument ~~results result to be~~ very robust and can operate
149 in a wide temperature range, between -40° and 85°C . A more detailed technical description of the
150 instrument can be found in Almansa et al. (2017; 2020).

151 The zenith sky radiance measurements at all channels are made simultaneously, providing an
152 output signal in analogic-to-digital units (ADU) every minute. This output is the computed average of 30
153 samples taken within the minute. ~~For each measurement, it is also,~~ ~~providing also aa variability~~
154 ~~parameter error~~ (ZEN ~~error variability~~) ~~associated to the measurement that describes both the atmospheric~~
155 ~~variability and the noise of the ZEN-R52~~ ~~within the minute of measurement, which is calculated as~~ ~~which~~
156 ~~is~~ the standard deviation of the 30 samples.

157 2.2 GRASP methodology

158 GRASP contains mainly two independent modules: the ‘forward model’ and the ‘numerical
159 inversion’. The first one is a radiative transfer model (RTM) used to simulate atmospheric remote sensing
160 observations for a characterized atmosphere. The second module, based on the multi-term least squares
161 method (Dubovik and King, 2000), is used in combination with the RTM for a statistically optimized fitting
162 of the observations to retrieve aerosol properties from radiometric measurements (Dubovik et al., 2014).
163 This provides the algorithm with high flexibility since different constrains can be applied to the retrieval
164 and can be modified ~~in order to~~ adapt the retrieval ~~for~~ each specific situation. It is important to mention
165 that GRASP works with normalized radiances (I_{GRASP}), which are related with the measured radiances as:

$$166 I_{GRASP} = I_{meas} * \pi/E_0 \quad (1)$$

167 Where I_{meas} is the radiance measured by the instrument and E_0 is the extraterrestrial solar
168 irradiance, both expressed in the same units. The standard ASTM-E490 solar spectrum has been used in
169 this work for the normalization of Eq. (1). This spectrum was calculated for moderate solar activity and
170 medium Sun-Earth distance; therefore, it has been corrected from Sun-Earth distance for each day of the
171 year. This way, the normalization factor must be applied when using data in radiance units as input to
172 GRASP and to transform the output normalized radiances from GRASP into radiance units.

173 2.2.1. Forward module

174 The GRASP forward module is a RTM based on the Successive Orders of Scattering approach
175 (Lenoble et al., 2007; Herreras-Giralda et al., 2022) which requires information about aerosol, gas, site
176 coordinates and date-time together with the solar zenith angle (SZA) to characterize the atmosphere
177 scenario. In this study, gases and aerosol information are extracted from AERONET direct and inversion
178 products available at Valladolid station. For the ~~gases-gases~~, it has been used the gases optical depth (GOD),
179 ~~while f~~For the used the aerosols, ~~information~~ has been used the size distribution (in 22 log spaced bins
180 of radius), sphere fraction and complex refractive indices at 440, 675 and 870 nm. Complex refractive index
181 at 500 nm has been interpolated from the values at 440 and 675 nm. The bidirectional reflectance
182 distribution function (BRDF) data is also used as input in GRASP. In this case The used the BRDF values
183 are extracted from an 8-day climatology created for the place of study using satellite data; specifically,
184 the MCD43C1 product from MODIS V005 collection (Schaaf et al., 2011) for the 2000–2014 period (see
185 Román et al. 2018 for more details about these climatology values).

186 The ZSR has ve been simulated at 440, 500, 675 and 870 nm with the GRASP forward module
187 using all the mentioned input data whenever it was available. These simulations have been used for
188 calibration purposes as can be observed in Section 3, but also for the sensitivity analysis with synthetic data
189 of Section 4.2. ZSR simulations are also performed for Section 4.1, but in this case the aerosol properties
190 have been obtained for precalculated aerosol types instead of real data from AERONET.

191 2.2.2 Inversion strategy

192 The present study aims to retrieve aerosol properties with GRASP using as input the calibrated
193 ZSR from the ZEN-R52 at four effective wavelengths. The versatility of GRASP allows different
194 approaches to model aerosols ~~in order to~~ maximize the possibilities of the different retrieval schemes.
195 Due to the reduced amount of information produced by the ZEN-R52, the approach called ‘models’ has
196 been chosen (Chen et al., 2020). This is a simple and fast processing approach where aerosol is assumed to
197 be an external mixture of several aerosol models. In this case, the approach assumes five aerosol types
198 which correspond to the typical aerosols on Earth: smoke, urban, oceanic, dust and urban polluted. Each
199 model has ~~a~~ fixed particle size distribution (log-normal for fine and coarse modes), refractive
200 ~~indices~~ indices, and sphere fraction, containing the already pre-calculated phase matrix, and the extinction
201 and absorption cross-sections (see Fig. S1 ~~1~~ for a representation of the size distribution ~~of~~ each model).
202 This way, the inversion strategy retrieves only five independent parameters: the total aerosol volume
203 concentration and the fraction of four models in the mixture (the fifth fraction equals one minus the rest of
204 the fractions). All these retrieved parameters allow to obtain other complex aerosol properties, like size
205 distribution parameters, weighting the individual properties of each model, which are known, by their
206 fraction ~~of~~ the mixture. The size distribution of the five models is defined for fine and coarse modes, hence
207 the retrieved parameters are also calculated for these modes. Then, ~~T~~the obtained size distribution

208 parameters ~~that can be obtained~~ are volume median radius of fine (RF) and coarse (RC) modes, standard
209 deviation of lognormal distribution for fine (σ_F) and coarse (σ_C) modes, and aerosol volume concentration
210 for fine (VCF) and coarse (VCC) modes and the total value (VCT). AOD ~~can be also calculated and it is~~
211 ~~given at for~~ each wavelength ~~is given~~ directly in ~~the~~ GRASP output. Each output, one per retrieval, provides
212 the relative residual differences between the measured ZSR (input) and the ones generated after the
213 inversion (simulated by GRASP forward module under the retrieved scenario) for each wavelength ([Román](#)
214 [et al., 2022](#)). This residual information will be used to evaluate the goodness of the retrievals, ~~rejecting~~
215 ~~the if the residual at one or more wavelengths is above an established threshold, the inversion is rejected~~
216 ~~(assumed as non-convergent) ones. This threshold, which varies with the wavelength, has been set as the~~
217 ~~absolute value of the accuracy plus the precision for each channel of the ZEN-R52 (see Section 3.5.2).~~

218 This proposed strategy requires as input: the calibrated ZSR at four wavelengths, the coordinates
219 of the site, date, time, SZA, the BRDF values obtained from the climatology mentioned above, and the
220 GOD at each wavelength to account for gases effect. The GOD used in this work is obtained from a monthly
221 GOD climatology, which has been created using GOD ~~data information retrieved~~ ~~extracted~~ from
222 AERONET for the 2012-2021 period in Valladolid ~~for this study~~. This proposed inversion strategy to
223 retrieve aerosol properties with GRASP using ZEN-R52 measurements has been named as ‘GRASP-ZEN’.

225 3. Calibration

226 A methodology for the ZEN-R52 calibration is proposed in this Section. This methodology ~~is can be~~
227 ~~developed using only~~ ~~a field~~ ~~measurements, so it campaign which does would~~ not require laboratory
228 measurements ~~except for the dark signal characterization. It, and it~~ is based on four steps: dark signal
229 correction, quality data filtering, temperature correction, and a final comparison against simulated values
230 to convert the output signal from ADU into radiance units ($\text{Wm}^{-2}\text{nm}^{-1}\text{sr}^{-1}$). With this purpose ZSR
231 simulations have been performed for the whole dataset of ZEN-R52 measurements ([April 2019 to](#)
232 [September 2021](#)), using the GRASP forward module fed with the closest AERONET information (Section
233 2.2.1) whenever it was available within ± 5 minutes from the ZEN-R52 measurement; considering in good
234 approximation, ~~and as checked later~~, that aerosol conditions ~~will do~~ not change significantly within 5
235 minutes. ~~To ensure the quality of the simulations, Only only those~~ AERONET retrievals with a sky error
236 lower than 5% have been used, ~~to ensure the quality of the simulations~~, obtaining a total of 4725 data pairs.

238 3.1. Dark signal correction

239 For the dark signal (DS) evaluation, the instrument was fully covered with a black piece and
240 introduced into a thermal chamber in the GOA-UVa facilities. The instrument was subjected to a
241 temperature variation in the range from -10 to 50 $^{\circ}\text{C}$ in darkness conditions. The dark signal registered by
242 each channel at each temperature is shown in Figure 1. It shows a constant behaviour for 440 and 500 nm
243 filters. ~~On the C~~ontrary, for the other wavelengths a ~~stepped-staggered~~ exponential behaviour can be seen.
244 ~~In order to To~~ characterize this behaviour, the logarithm of the ZEN dark signal has been fitted to a three-
245 degree polynomial. This fitting is after rounded up to the unit to obtain a ~~stepped-staggered~~ fitting. The
246 modelled dark signal is also represented in Figure 1 by the black lines. This modelling has been used to
247 subtract the corresponding dark signal value to the raw signal, obtaining dark signal corrected ZSR
248 (ZSR_{DSC}). ~~The residuals between the modelled and real DS are shown in the supplementary material (Figure~~
249 ~~S2); these residual values are within the instrument resolution for all channels. Details of the fitting and a~~
250 ~~residuals graph has been included in Figure S2 in the supplementary material, where it can be appreciated~~
251 ~~a good correlation between the modelled DS and the real DS. It has also been verified that the dark signal~~
252 ~~behaviour has remained constant over time, comparing the modelled DS against the night-time~~
253 ~~measurements. In this work, the~~ The DS signal has been characterized in the laboratory ~~in this work in order~~
254 ~~to to~~ cover a ~~high-wide~~ range of temperatures, but it could be calculated from the night-time measurements
255 (dark sky) ~~or even from day-time measurements (covering the instrument with a black piece)~~, ~~when a~~
256 thermal chamber is no available.

257 3.2 Quality control filtering criteria

258 With the dark signal corrected, we compared ~~the~~ the field measurements of ZSR_{DSC} against the
259 ~~simulated~~ ZSR ~~simulated values~~ (ZSR_{SIM}). This ~~first~~ comparison is shown in ~~left panels in~~ Figure 2. The

260 colour of the points in the scatter plots of Figure 2 represents the density of points per pixel as
 261 defined by Eilers and Goeman (2004), using a $\lambda=50$ for smoothness; all the density scatter plots of this
 262 paper were done in this manner with the same configuration. The determination coefficient (r^2) is also added
 263 in the panels of Figure 2, showing in general good agreement for each channel between ZSR_{DSC} and ZSR_{SIM}
 264 but with some outliers regarding the linear trend (see left panels a, c, e and g). These outliers present higher
 265 ZSR_{DSC} values than expected and they could be caused by the presence of clouds in the zenith, instrument
 266 malfunction and others.

267 The ZEN-R52 measurements can be affected in different ways. For example, a possible sun stray-
 268 light intromission when sun is very elevated can increase the measured signal, clouds presence can also
 269 affect it, or the variation in temperature can introduce some dependency. To identify and reject the cloud-
 270 contaminated or wrong measurements, different thresholds have been identified after the visual analysis of
 271 some parameters in the scatter plots several parameters have been considered in this subsection: SZA, ZEN
 272 error, temperature, and the time interval between the inversion used to simulate the ZSR_{SIM} and the
 273 corresponding ZSR_{DSC}. Some thresholds have been identified after the visual analysis of these parameters
 274 in the scatter plot. For the SZA, the signal of the ZEN instrument is higher than the expected for SZA values
 275 below 30°, which could be explained by some sun stray-light intromission coming to the sensors due
 276 to the high elevation of the Sun. Then, ZSR_{DSC} values recorded under SZA below 30° have been discarded,
 277 and but also the values with SZA above 80° due to the low signal registered for this SZAs (See Figure S32
 278 for a clear overview). The ZEN error variability parameter (Section 2.1.3) can be assumed as a cloud
 279 presence indicator, since measurements affected by clouds should register a high ZEN error variability due
 280 to the high variability fluctuation of the sky radiances during the 1-min measurement. An evaluation of
 281 Figure 2 but with points classified by its ZEN error variability at 440 nm led us to establish a threshold of
 282 4% for this parameter e ZEN error inat the four channels (See Figure S34). If the measurement of any
 283 channel has a ZEN error above this threshold, then the measurements of the four channels are rejected.

284 No other clear dependence of the outliers on the rest of the parameters has been observed. The
 285 results after applying the mentioned filters (30° < SZA < 80°; ZEN error variability < 4%) are represented
 286 in the right panels (b, d, f and h) of Figure 2. The number of coincident measurements is reduced to 4369
 287 points after applying the quality control but a significant improvement in the determination coefficients is
 288 observed, rising from 0.967, 0.93, 0.85 and 0.8 to 0.99, 0.99, 0.96 and 0.95 to 0.99 for the 440, 500, 675
 289 and 870 nm channel and from 0.80 to 0.95 in the case of 870nm respectively. From now on, all the ZSR_{DSC}s
 290 measurements will used will be assumed to satisfy this quality control unless otherwise specified.

291 3.3 Temperature correction

292 In order to check the dependence with temperature of each filter channel the ratio ZSR_{DSC}/ZSR_{SIM}
 293 ratio normalized by the mean ratio is has been plotted against the temperature in Figure 3. In the left panels
 294 (a, c, e and g) of Figure 3 all data points are represented together with the linear fit, showing a constant
 295 behaviour negligible dependence on temperature dependency for 440 and 500 nm. For, but a clear trend for
 296 675 and 870 nm channels this dependency must be considered, since nm channels they presents slopes of
 297 the linear fitting of 0.008 °C⁻¹ and 0.0036 °C⁻¹, respectively. These values are higher than compared to
 298 the 0.0002 °C⁻¹ obtained for the other two channels, which led us to consider a temperature correction for
 299 675 and 870 nm. In order to despise disregard outliers, the ratios were grouped by 2 °C bins and its median
 300 was calculated whenever the group had at least 40 points. These median values are plotted against the mean
 301 temperature of the group's temperatures in Figure 3 right panels (b, d, f and h). The corresponding linear
 302 fit coefficients obtained in Figures 3f and 3h has been established to be used to correct the ZSR_{DSC} at 675
 303 and 870 nm applying the next are used for the temperature dependency correction following Equation 2:

$$304 \quad ZSR_{TC}(\lambda) = \frac{y_{20}(\lambda)}{a(\lambda)+b(\lambda)T} ZSR_{DSC}(\lambda); \lambda = 675, 870 \text{ nm} \quad (2)$$

305 where ZSR_{DSC} is the ZEN signal after dark signal correction and ZSR_{TC} is this signal with the temperature
 306 correction applied; a and b represent the intercept and slope of the final linear fits, respectively; y_{20} is the
 307 correspondent y-axis value of the linear fit at the temperature T of 20 °C (arbitrary value chosen to
 308 normalize). For 440 and 500 nm ZSR_{DSC} and ZSR_{TC} are equivalent since no temperature correction is
 309 applied. This temperature correction is only applied to the λ wavelengths of 675 and 870 nm.

310 3.4. Calibration coefficients

311 The calibration factors can be directly obtained by comparing the dark and temperature corrected
312 ZSR from the ZEN-R52 against the values simulated by GRASP. Once the dark signal correction, quality
313 filtering and temperature correction are applied to the ZEN-R52 raw signal, the definitive comparison
314 between the ZSR from the ZEN-R52 and the ZSR values simulated by GRASP forward module can be
315 done to obtain the calibration coefficients. The density scatter plots between ZSR_{SIM} values and ZSR_{TC} are
316 shown in Figure 4. The slope of the linear fit directly represents the calibration coefficients obtained to
317 transform the ZSR_{TC} signal into radiance units ($Wm^{-2}nm^{-1}sr^{-1}$) for each channel. Theis calibrated ZSR
318 radiance isare named ZSR_{ZEN} hereafter.

319 These obtained calibration coefficients are compared toand the ones obtained by intercomparison
320 with a calibrated integrating sphere at IARC facilities are shown in Table 1. Table 1 also presents the
321 relative differences between both calibration coefficients using the coefficients from IARC as reference;
322 the uncertainty involved in the latter calibration method procedure is estimated to be 5% by Walker et al.
323 (1991). These differences are 1.39%, -6.54%, -6.72% and -5.89% for 440, 500, 675 and 870 nm,
324 respectively. The proposed calibration method uses the standard ASTM-E490 solar spectrum for
325 transformingto transform the unitless output radiances from GRASP, as indicated in Equation 1. This fact
326 can increase the relative differences between the two calibration methods, together with the lack of
327 temperature correction in the second one. However, when using ththe e-calibration method employed
328 heredeveloped in this study, allows to use the same normalization factor applied to the ZSR simulated by
329 GRASP (ZSR_{SIM}) can be applied that lately will be applied to the calibrated ZEN-R52 ZSR_{ZEN}
330 measurements when using them as inputthat will be introduced in the to GRASP for the inversion module,
331 This way it can be avoided avoiding tothe introduction of a systematic error due to the normalization
332 required by theGRASP inversion algorithm. It means that this calibration method is better suited when
333 using the ZSR_{ZEN} values as input for GRASP to retrieve aerosol properties, since there is no need for
334 extraterrestrial spectrum normalizationwe could work directly with the normalized radiances from GRASP.
335 For this work, it has been assumed that during the period of study the calibration has not decayed, since it
336 is not a long dataset. Nevertheless, a recalibration must be considered, especially if there is any maintenance
337 or repair task. From now on ZSR_{ZEN} will stand for the calibrated zenith sky radiances measured by the
338 ZEN-R52 satisfying the stablished quality controls ($30^{\circ} < SZA < 80^{\circ}$; ZEN error-variability < 4%).

339 3.5. ZEN-R52 vs. CE318 photometer comparison

340 In order to check the goodness of the calibrated ZEN-R52 measurements, the ZSR_{ZEN} observations
341 have been compared with-against measurements recorded by collocated CE318 instruments for the whole
342 available dataset of ZEN-R52 measurements (April 2019 to September 2021). For the comparison,
343 independent measurements extracted from CE318 photometers forfrom two different scenarios are
344 employedused: the cloud mode (CM) and the principal plane scanning (PPL).

345 3.5.1. Cloud Mode

346 The CE318 sun-sky photometer allows to perform measurements in the ‘cloud mode’ scenario. It
347 is carried out when the direct sun measurement indicates an obscured sun, and therefore the aerosol retrieval
348 is not possible. This scenario orientates the sensor head into the zenith direction and takes zenith radiance
349 measurements at 9 s intervals for each wavelength, which are obtained by successively rotating an
350 interference filter in front of the detector. The ‘cloud mode’ scenario was originally implemented to obtain,
351 during this idle time, cloud optical depth from zenith sky radiances at the spectral wavelengths employed
352 by the sun-sky photometer (Chiu et al., 2010) as suggested by Marshak et al. (2000) and Barker and
353 Marshak (2001).

354 The zenith sky radiances measured under the cloud mode (ZSR_{CM}) have been directly downloaded
355 from the AERONET network webpage. For the comparison with ZEN-R52, quasi-coincident (the closest
356 within ± 1 min) ZSR_{ZEN} and ZSR_{CM} measurements have been obtained-paired and plotted in Figure 5,
357 showing a good correlation between both datasets. The deviation between them is high, likely due to the
358 short-time variation in the cloud radiative field. Figure 5 includes all the ZSR_{ZEN} measurements; the filtering
359 to SZA values and ZEN errors-variability is not applied, since the cloud mode measurements is under cloud
360 presence. In this case, there is not dependence on SZA; outliers do not appear for $SZA < 30^{\circ}$ values. Hence,
361 the ZSR_{ZEN} values do not correlate with reference valuesare only wrong for $SZA < 30^{\circ}$ when the sun is
362 cloud-free, which confirms the suggested explanation that ZSR_{ZEN} measurements are contaminated by stray
363 sun light under cloud-free conditions when the sun elevation is high ($SZA < 30^{\circ}$). In addition, it was checked

364 that 86% of the ZEN-52 measurements used in this comparison (which are known to be affected by clouds),
365 present a ZEN ~~error~~-variability > 4% at least for one channel. This also validates the proposed use of the
366 ZEN ~~error~~-variability as a rough ‘cloud screening’.

367 ~~This -CM-comparison against the cloud mode measurements will not be used to quantify the~~
368 ~~uncertainty of the ZEN measurements; it is because, -since clouds are very variable and, therefore, the~~
369 ~~recorded signal. Therefore, we should need to compare both measurements carried out at exactly the same~~
370 ~~time; but this is not the case since ZEN measurements are 1-min averages while CE318 photometer~~
371 ~~measurements are quasi-instantaneous. In addition, Ffor the retrieval of aerosol properties, it is necessary~~
372 ~~to employ measurements under cloud-free conditions from clear sky, not contaminated by clouds, -~~
373 ~~tTherefore, the results obtained in following comparison will be the reference ones.~~

374 3.5.2. Principal plane scan

375 CE318 sun-sky photometers allow to perform three different scanning scenarios for sky radiance
376 measurements. One of these scanning scenarios is ~~in~~ the principal plane (PPL) geometry, where the azimuth
377 angle is equal to the solar azimuth angle while the zenith angle varies measuring sky radiances ~~at the same~~
378 ~~fixed angles regards the SZA~~. This is done sequentially once for each channel starting at 870nm, followed
379 by 675, 500 and 440 nm channels for each PPL scenario. The PPL geometry allows to extract the ZSR by
380 linear interpolation of the PPL points to the zenith position. ~~A In this situation, the~~ cloud screening of PPL
381 points has been made checking the smoothness of the PPL curve as described in Holben et al. (1998). The
382 smoothness criterion analyses the second derivative of the PPL radiances with respect to the scattering
383 angle. This way the PPL measurement is classified as cloud contaminated if the second derivative is
384 negative (the threshold is not 0 but -1×10^{-7} as empirically determined) at any scattering angle between 2
385 and 90° (Almansa et al., 2020). The obtained ZSR from this method, based on the interpolation of cloud-
386 screened CE318 sky radiances measured in the PPL geometry, has ~~ss~~ been labelled as ZSR_{PPL}.

387 The PPL dataset is not directly available in the AERONET webpage; then, it has been extracted
388 from CAELIS database (Fuertes et al., 2018; González et al., 2020). ZSR_{ZEN} and ZSR_{PPL} measurements
389 within ± 1 min, are compared in Figure 6. Upper panels (a-d) of Figure 6 show the density scatter plots of
390 ZSR_{ZEN} against the reference ZSR_{PPL}, where a high correlation between both datasets can be observed for
391 all the channels, varying the determination coefficients ~~from-between~~ 0.94 (at 870 nm) ~~to~~ and 0.99 (at 440
392 and 500 nm). In general, the number of outliers is higher for longer wavelengths.
393 In order to evaluate the uncertainty of the ZSR_{ZEN} measurements using ZSR_{PPL} as reference, the relative
394 differences between ZSR_{ZEN} and ZSR_{PPL} (Δ ZSR_{ZEN-PPL}) have been evaluated and represented in frequency
395 histograms in the bottom panels (e-h) of Figure 6. These panels also include the mean (mean bias error;
396 MBE), median (Md) and standard deviation (SD) of Δ ZSR_{ZEN-PPL}. The median values, less sensitive to
397 outliers, are close to zero (Md = 1.36%, -1.39% and -0.22% for 440, 500 and 675 nm, respectively)
398 indicating that the ZSR_{ZEN} are accurate regarding the reference ZSR_{PPL} values, except for 870 nm channel,
399 ~~which-whose~~ Md value of 4.99% points out an overestimation of the reference ZSR values. ~~Nevertheless,~~
400 ~~t~~The precision decreases for longer wavelength channels, from SD values of 3.00% and 4.62% for 440 and
401 500 nm, respectively, to SD=12.54% and 21.37% for 675 and 870 nm. ~~These accuracy and precision values~~
402 ~~will be used in the convergence criteria mentioned in Section 2.2.2.~~

403 All these statistical parameters have been calculated also considering the calibration coefficients,
404 without temperature correction, obtained at IARC with a calibrated integrating sphere. These parameters,
405 and the previously obtained by the proposed method of this work, are shown in Table 2 ~~in order to observe~~
406 ~~check~~ which calibration provide ZSR values closer to the reference ZSR_{PPL} values. The results of Table 2
407 show that the ZSR obtained with the proposed calibration method, based on intercomparison with ZSR
408 simulations, ~~is,~~ in general, more accurate and precise except for 440 nm. Although the results of Table 2
409 for 440 nm are worse for the proposed calibration than for IARC calibration, the results are still good for
410 the proposed method with MBE close to 0 (1.96 % respect 0.73% for IARC) and a low value of SD (3%
411 respect 2.95% for IARC). The ZSR_{ZEN} values from IARC calibration are not temperature corrected, which
412 could ~~be behind of part of~~ partially explain the observed differences.

413 ~~All these~~These results indicate that the ~~ZSR_{ZEN}-ZEN-R52 measurements at 440 and 500 nm values are~~
414 ~~more accurate and precise than at 675 and 870 nm. Then, ZSR_{ZEN} measurements are more reliable~~ at shorter
415 wavelengths, ~~and, therefore,~~ should ~~have more weight~~ be given more importance than those corresponding
416 to longer ones in the aerosol-retrieval of aerosol properties ~~than the measured for longer ones, since~~

417 ~~measurements at 440 nm and 500 nm are more trustable.~~ The inversion module from GRASP code ~~takes~~
418 ~~into account~~ considers the ~~weight importance~~ of each measurement through the so-called ‘noises’; allowing
419 to associate a different ‘noise’ or reliability to each channel, ~~considering them as normal distributions in~~
420 ~~this case.~~ Therefore ~~The,~~ the obtained standard deviations ~~collected in~~ of Table 2 (using the calibration
421 proposed in this work), associated with the ZSR_{ZEN} uncertainty, ~~are used to this end will be introduced for~~
422 ~~each channel in GRASP for the~~ GRASP-ZEN method ~~to account for the different reliability of each~~
423 ~~channel.~~

424 4. Sensitivity analysis

425 In order to analyse the capabilities of the proposed inversion strategy to invert ZSR_{ZEN} measurements
426 with GRASP, a detailed sensitivity analysis is carried out in this section using synthetic data.

427 As mentioned in Section 2.2.2, the chosen method to obtain aerosols properties, considers five aerosol
428 types or ‘models’, which have fixed size distribution, refractive indices and sphere fraction. The method
429 must retrieve aerosol properties from measurements of ZSR_{ZEN} at 440, 500, 675 and 870 nm, ~~which is a~~
430 ~~limited information.~~ Sky radiances depend on aerosol concentration and type, among other factors like the
431 scattering angle and SZA; hence they are commonly used to retrieve aerosol properties by measuring them
432 at different scattering angles and wavelengths (Nakajima et al., 1996; Román et al., 2022). Figure S45
433 shows, in the supplementary material, the sky radiances in the zenith direction, modelled by GRASP for
434 different aerosol concentrations, and how they are sensitive to changes in the AOD and aerosol type for the
435 five aerosol types used by the inversion method. This figure shows that for higher SZA (Figure S45; panels
436 i-l) the ZSR values are less sensitive to aerosol type and concentration, since different scenarios show
437 smaller differences in the corresponding ZSR, ~~due to the lower signal in these conditions.~~ Nevertheless, for
438 lower SZA conditions (Figure S45; panels a-d) ~~show there is~~ a clear sensitivity to type and aerosol load for
439 AOD at 440 nm, ~~at least for values below~~ 0.7; ~~limit that values above 0.7 would represent~~
440 ~~characterizes~~ are assumed for and extreme AOD events (Mateos et al., 2020) ~~and therefore is~~ are unusual.

441 To explore the limitations of the retrieval of aerosol properties following the proposed inversion
442 strategy, two different tests have been carried out. For both tests, ~~artificial synthetic~~ aerosol scenarios have
443 been created and used as input to the GRASP forward module to simulate the ZSR ~~that the ZEN-R52 would~~
444 ~~register~~ under these ~~synthetic~~ scenarios (ZSR_{SYN}). Since the ZSR_{SYN} values are ~~artificially manually~~
445 ~~and not real measurements~~, they will be randomly perturbed following a Gaussian distribution defined by
446 the uncertainty of each channel previously calculated for the ZEN-R52 to create realistic observations
447 (similar to Torres et al., 2017 and Román et al., 2022, among others). The perturbed ZSR_{SYN} will be then
448 used as input ~~for~~ in the inversion module, following the GRASP-ZEN method. It will provide the ~~retrieved~~
449 aerosol properties as output, which will be labelled with the subindex ‘INV’ referring to ‘inversion’. The
450 test ~~will be~~ is focused on the ~~capability to retrieve~~ retrieval of AOD ~~values~~ and size distribution properties.

451 4.1. Scenarios from the combination of five aerosol types

452 In ~~thi~~ This test ~~the creates random synthetic~~ aerosol scenarios ~~are~~ formed by a ~~random~~ mixture of
453 the five aerosol types used by the ‘models’ GRASP inversion strategy (see Section 2.2.2). ~~We aim h~~ Here
454 ~~we aim~~ to assess the capabilities of the retrieval of aerosol properties if the observed aerosol ~~wasis~~ actually
455 a pure mixture of these five types of aerosol. To this end, ~~random fractions of~~ each aerosol type ~~are~~
456 ~~selected together with~~ are selected together with ~~aa~~ random ~~total~~ aerosol concentration chosen in the interval
457 from 0.01 to 0.15 $\mu\text{m}^3/\mu\text{m}^2$, ~~which will be used in combination with the fixed aerosol properties from each~~
458 ~~model.~~ creating a total of 1000 scenarios. The simulations have been made for three different SZA ~~values~~
459 (30, 50 and 70°), but we will focus here in the SZA=50° situation, which would represent a half-way and
460 common scenario for the latitude of Valladolid.

461 Figure 7 shows the ~~retrieved AOD (AOD_{INV} retrieved), using as input the perturbed ZSR_{ZEN} of~~
462 ~~each created random scenario~~ for SZA equal to 50°, against ~~its the~~ original synthetic AOD ~~value~~ (AOD_{SYN}).
463 The same graphs for SZA ~~values of~~ at 30° and 70° are shown in the Figure S65 of the supplementary
464 material. In general, the data deviation increases for high AOD values, which are less frequent. For SZA
465 equal to 50°, the method overestimates the aerosol load for all the wavelengths, with MBE ranging from
466 0.23 ~~at 440 nm~~ to 0.11 ~~at 870 nm~~. The best results are obtained for SZA = 30°, with absolute mean bias
467 errors lower than 0.002 for all wavelengths and the lowest uncertainty (standard deviation lower than 0.66);
468 while for SZA = 70° the method slightly underestimates the AOD with MBEs ranging from -0.004 to 0. It
469 is important to point out that the convergence capability of the method decreases for high SZAs, being the

470 convergent inversions a total of 43.2% and 43.6% at SZA=30° and 50° respectively but only 27.1% for
471 SZA=70°; considering that there are initially 1000 scenarios. These results could be related to the
472 dependence of the ZSR sensitivity on the SZA, which is higher for lower SZA, and therefore would make
473 easier for the method to find a solution.

474 For the size distribution the frequency histograms of the absolute differences between the inverted
475 and the synthetic parameters are shown in Figure 8 to have for a clear overview of the results obtained (the
476 direct scatter plot comparison can be seen in Figure S76). For the current synthetic test, the retrieval
477 of size distribution properties is very accurate and precise, showing Md values very close to zero for all the
478 properties. For the volume median radius and standard deviation of the lognormal distribution the precision
479 is high, with SD < 10% for both fine and coarse modes. In the case of but the precision is worse for the
480 aerosol volume concentration the uncertainty is higher, with an SD values of about 0.03 (34.63%), 0.01
481 (20.4%) and 0.02 $\mu\text{m}^3/\mu\text{m}^2$ (53.9%) for the total, fine and coarse respectively concentration. These results
482 could be explained, at least in part, due to the fixed size distributions for the 'models', which present similar
483 RF, RC, σF and σC values and, therefore, it will not show an important variation when combining them,
484 but contrary, the aerosol volume concentration is an extensive property and therefore can have a higher
485 variation.

486 4.2. AERONET scenarios

487 The same procedure than in the previous test is developed in this test one but using realistic aerosol
488 properties scenarios retrieved at Valladolid by AERONET. In this case, the AERONET retrieved aerosol
489 properties (size distribution, refractive indices, etc.) are used directly as input for in the GRASP forward
490 module to simulate the ZSR values. For this new test, all the available inversions (almucantar and hybrid
491 scans) from AERONET for the coincident ZEN-R52 measurement period (2019-2021) with and sky error
492 < 5% have been used obtained, achieving obtaining a total of 5321 synthetic scenarios. With this test we
493 aim to assess the capabilities of the method to retrieve the aerosol properties when the ZSR come from an
494 aerosol scenario correspond to closer to real aerosol conditions and not necessarily to a mixture of the five
495 mentioned aerosol types. In this situation the ZSR_{SYN} simulations are made for the corresponding date and
496 time at which the AERONET inversion product was retrieved, achieving a wide variety of SZA values (18°
497 \leq SZA \leq 78°).

498 Figure 9 presents the comparison between the AOD_{INV}, obtained from the inversion of the
499 perturbed ZSR_{SYN} as input in with GRASP-ZEN method, and AOD_{SYN} from for these AERONET synthetic
500 scenarios. This comparison reveals a clear overestimation of the inverted AOD values compared to the
501 original ones for the four wavelengths, ranging the MBE values from 0.01 to 0.04 and the Md from 0.01 to
502 0.03 for the differences between both datasets. These results could be related with the previous results of
503 AOD for overestimated AOD_{INV} at SZA = 50°, but in this situation the overestimation it is not related
504 with the SZA, since it has been checked that points with different SZA are homogeneously distributed. Therefore,
505 AOD_{SYN} is always the overestimated one occurs by the obtained from GRASP-ZEN for all SZA.
506 The standard deviation of the AOD differences, which can be associated with a 'theoretical uncertainty'
507 in AOD_{INV} of the method, is above 0.02, being 0.05 for 440 and 500 nm, 0.03 for 675 nm, which are higher
508 than the standard deviation obtained in the previous section for all wavelengths and SZAs, SD = 0.090 (for
509 AOD 440 nm at SZA = 50°) and 0.02 for 870 nm.

510 The reason for the observed overestimation could be in the limitations of the GRASP-ZEN method
511 based on the 'models' approach, which only allows to retrieve aerosol properties within the properties of
512 the five aerosol types. It means that, for example, if the real aerosol has a median radius of fine mode bigger
513 than the ones of the five 'models', then the GRASP-ZEN retrieval will underestimate the real median radius
514 of fine mode and this difference will be compensated unbalancing other aerosol properties to fit the
515 measured ZSR and the synthetic ZSR values of the retrieved aerosol scenario (to reduce the residual
516 differences in ZSR values).

517 To explore this hypothesis, the retrieved size distribution properties have been compared with the
518 synthetic ones. The frequency histograms for the absolute differences between the inverted and the
519 synthetic properties are shown in Figure 10 (the direct scatter plot comparison can be seen in Figure S78).
520 The retrieved volume concentrations present median differences regarding the synthetic ones about 0.01
521 $\mu\text{m}^3/\mu\text{m}^2$ for VCF and VCT, while this median value is and very close to zero for the VCC. Similarly to the
522 AOD, the volume concentration present a theoretical uncertainty of 0.01 $\mu\text{m}^3/\mu\text{m}^2$ for the fine mode and
523 0.02 $\mu\text{m}^3/\mu\text{m}^2$ for coarse mode and the total. The retrieved fine-intensive properties underestimate the

524 reference values, being the median values of their differences about -14% and -10% for RF and σ_F ,
525 respectively, and -10% and -4% for RC and σ_C , respectively.

526 This lack of accuracy is the main difference between the results of Figure 10 and Figure 8. As
527 mentioned before, we would expect a [higher big](#) accuracy and precision in the retrieved values of the volume
528 median radius and standard deviation for the ‘models’ combination scenarios test (Section 4.1), since the
529 scenario can be perfectly reproduced by GRASP-ZEN because it is a combination of the same models used
530 in the inversion module; however, for a real aerosol scenario (the test for AERONET scenarios of this
531 subsection), these properties could be impossible to obtain with enough accuracy since they present wider
532 range of size distributions than the offered by the ‘models’ approach. Similar results are expected for the
533 real and imaginary refractive index and other optical properties, due to the limitations of the ‘models’
534 approach.

535 The results of this section conclude that the GRASP-ZEN method is useful for the retrieval of
536 AOD but not for some size distribution properties, like the volume median radius and standard deviation
537 of fine and coarse modes. Therefore, we will focus on the retrieval of AOD at 440, 500, 675 and 870 nm
538 and VCF, VCC and VCT.

539 5. [Results GRASP-ZEN application to ZEN-R52 database](#)

540 Once the ZSR_{ZEN} measurements have been ~~obtained from ZEN-R52 by the calibration method~~
541 [proposed in Section 3 calibrated](#), and the GRASP-ZEN method has been proved in Section 4 as capable to
542 retrieve ~~some~~ aerosol properties ~~like AOD~~, the GRASP-ZEN methodology has been applied to ~~all the~~
543 [whole the](#) available dataset ~~from of~~ ZEN-R52 measurements at Valladolid [at the moment of the study](#). ~~As~~
544 [result obtaining a a](#) total of 222663 GRASP-ZEN retrievals [have been obtained between April 2019 and](#)
545 [September 2021](#). This dataset has been obtained using ZSR_{ZEN} measurements which satisfy the filtering
546 criteria, ~~regarding SZA and ZEN error~~, determined in Section 3.2. The retrievals ~~which do not present~~
547 ~~enough considered as non-convergent~~ have been removed, which led to a total of 170637 retrievals. This
548 convergence check is based on [the evaluation of](#) the residuals ~~effrom~~ the inversion process (see Section
549 2.2.2). A cloud-screening filter is applied, based mainly on the retrieved AOD at 500 nm, following a
550 similar procedure as Giles et al. (2019) for cloud-screening in AERONET version 3. Three checks are
551 applied for this cloud-screening: smoothness, stand-alone and $\pm 3\sigma$. The smoothness check is done by the
552 analysis of the AOD variation at 500 nm: for each two subsequent values, if the variation is higher than
553 0.01/min the retrieval with larger AOD at 500 nm in the pair is removed. After the smoothness, the stand-
554 alone check is applied: all single retrievals ~~remaining~~ which are more than 1 hour apart from the closest
555 available retrieval are removed. Finally, for each day, the daily mean and standard deviation are calculated
556 for the retrieved AOD at 500 nm and for the Ångström Exponent (AE; Ångström, 1964) obtained with the
557 four retrieved AOD values (440, 500, 676 and 870 nm). To satisfy the $\pm 3\sigma$ check, the retrieved AOD at
558 500 nm and AE must be within the daily mean $\pm 3\sigma$ (triple standard deviation). Values not satisfying this
559 requirement are removed. A final dataset with 126112 points satisfying the convergence and cloud-
560 screening criteria is obtained.

561 5.1 Aerosol Optical Depth

562 The AOD retrieved by GRASP-ZEN using the ZSR_{ZEN} measurements (AOD_{GRASP_ZEN}) has been
563 compared against independent AOD measurements from AERONET ($AOD_{AERONET}$) derived from CE318
564 sun-sky photometers collocated with the ZEN-R52 at Valladolid. Figure 11 shows the complete time series
565 evolution of AOD_{GRASP_ZEN} together with $AOD_{AERONET}$, both at 440 nm. Despite some AOD_{GRASP_ZEN}
566 outbreaks which are not reproduced by the $AOD_{AERONET}$, both datasets show in general a similar temporal
567 evolution. Figure 12 shows a more detailed view of these data in a shorter period, from 16 to 22 June 2020,
568 with high availability of data from both GRASP-ZEN and AERONET datasets for the four [available](#)
569 wavelengths. A lack of AOD values in the GRASP-ZEN dataset around mid-day is observed; it is explained
570 by the rejection of ZEN-R52 measurements for SZA below 30° , which, in the analysed period and latitude,
571 occurs around mid-day. In Figure 12 (panels a–d) it can be also observed that both GRASP-ZEN and
572 AERONET datasets vary with time in a similar way for all the wavelengths, with AOD values from
573 GRASP-ZEN slightly overestimating the AOD values from AERONET at all wavelengths. [Figure 12 \(panel](#)
574 [e\) includes the \$AOD_{GRASP_ZEN}\$ at 440, 500, 675 and 870 nm in the same plot, showing the behaviour](#)
575 [expected for the AOD at these wavelengths: AOD decreasing with wavelength and parallel time evolution.](#)

576 To perform a more quantitative analysis of the correlation between these datasets, a match-up of
577 AERONET AOD ($AOD_{AERONET}$) ~~data~~ with GRASP-ZEN AOD (AOD_{GRASP_ZEN}) values within 1.5 minutes
578 has been made, obtaining a total of 37787 coincident points per wavelength. The AOD data from GRASP-
579 ZEN is represented against the coincident AOD from AERONET in a density plot in Figure 13 for each
580 wavelength (panels a- d). This figure (panels e-h) also shows in the bottom panels the frequency histograms
581 ~~for~~ the differences between both AOD datasets. AOD_{GRASP_ZEN} presents a higher correlation with
582 $AOD_{AERONET}$ for shorter wavelengths, ranging r^2 from 0.86 at 440 nm to 0.72 at 870 nm. In general, the
583 AOD at 675 nm, and especially at 870 nm, presents more deviation between the data pairs than for the
584 shorter wavelengths. Some outliers presenting high AOD_{GRASP_ZEN} values can be appreciated, especially at
585 shorter wavelengths; it could be caused by some spurious measurements likely contaminated by clouds that
586 pass the cloud-screening criteria, or recorded with dirtiness, rain droplets or dust over the instrument (it
587 must be frequently cleaned). AOD from GRASP-ZEN generally overestimates the AERONET values, as
588 ~~synthetic~~ ~~the sensitivity~~ study of Section 4.2 ~~pointeds~~ out, with median values of the differences of
589 AOD_{GRASP_ZEN} with respect to $AOD_{AERONET}$ between 0.01 and 0.02 for all wavelengths; similar values
590 appear for MBE, ranging from 0.01 to 0.03. The uncertainty in the retrieved AOD_{GRASP_ZEN} is estimated by
591 SD to be 0.03 for 440 and 500 nm and 0.02 for 675 and 870 nm using as reference the values provided by
592 AERONET, which are within the theoretical uncertainty obtained in the previous section for the AOD.

593 5.2 Aerosol volume concentration

594 Regarding the total aerosol volume concentration, the ~~retrieved~~ ~~values~~ retrieved with GRASP-
595 ZEN and the ~~obtained ones~~ from AERONET ~~along for~~ the ~~w~~ analysed hole period are shown in Figure
596 14. The time evolution shows generally a similar behaviour for both datasets with exception of some VCT
597 extreme values more frequent in the GRASP-ZEN database. Here it can be also seen that for this parameter
598 there is a higher temporal coverage from GRASP-ZEN than from AERONET. ~~This is because unlike the~~
599 ~~AOD, which is obtained from direct irradiance measurements, usually carried out every 3 minutes, the~~
600 ~~aerosol volume concentration is obtained from AERONET inversion products, which are retrieved from~~
601 ~~the combination of AOD and sky radiance measurements. Sky radiances are performed less frequently than~~
602 ~~the direct sun ones, and inversions are only processed if the sky measurements are available and satisfy~~
603 ~~certain requirements (Sinyuk et al., 2020).~~

604 The VCF , VCC and VCT values from both datasets are shown in Figure 15 for the week from 16
605 to 22 June 2020 (same days than Figure 12), showing again a similar behaviour for the two datasets. Figure
606 15 also reveals that the GRASP-ZEN values are noisier and ~~overestimates higher than~~ the AERONET
607 values, especially for the fine mode.

608 ~~In order to perform a~~ For a more quantitative analysis ~~for of~~ the correlation between VCF , VCC and
609 VCT from GRASP-ZEN and AERONET datasets a synchronization -with a time window of ± 5 min was
610 done, match up has been done. In this case, the GRASP-ZEN values closest to the AERONET values within
611 5 minutes are chosen, obtaining a total of 4356 coincident points for each volume concentration. A higher
612 temporal range is selected here because the inversion products are less frequent than AOD. In addition, we
613 assume that these aerosol properties should not change significantly in 5 minutes.

614 The GRASP-ZEN volume concentrations are represented against the coincident AERONET ones in
615 the density scatter plots of the upper panels of Figure 16 for fine, coarse and total values. Bottom panels of
616 Figure 16 also show the frequency histograms of the differences between GRASP-ZEN and AERONET
617 values of VCF, VCC and VCT. The best correlation is obtained for the total volume concentration, with a
618 r^2 of about 0.66, while for fine and coarse volume concentration the determination coefficients ~~is~~ are 0.57
619 and 0.56, respectively. Despite the lower correlation coefficients, the retrieved volume concentrations are
620 rather precise, with median values of values of the median of the differences between GRASP-ZEN and
621 AERONET datasets ~~about of~~ 0.006 and 0.005 $\mu\text{m}^3/\mu\text{m}^2$ for fine and coarse modes, respectively, and 0.010
622 $\mu\text{m}^3/\mu\text{m}^2$ for the VCT. The highest dispersion of the uncertainty differences in on the retrieved volume
623 concentrations ~~is~~ obtained for the VCT, which presents a SD value about 0.0200 $\mu\text{m}^3/\mu\text{m}^2$; while for
624 fine and coarse modes these values are 0.009 $\mu\text{m}^3/\mu\text{m}^2$ and 0.016 $\mu\text{m}^3/\mu\text{m}^2$, which are close to the
625 uncertainty ~~offered by of~~ AERONET products, 0.01 $\mu\text{m}^3/\mu\text{m}^2$. These results are again within the theoretical
626 uncertainty obtained in the previous section.

627 All ~~of~~ the results of this paper have been obtained using the GRASP-ZEN methodology based on the
628 'models' approach, which is a suitable option for the current ~~issue~~ study due to the reduced number of

629 radiometric observations provided by the ZEN-R52. However, the versatility of GRASP code allows
630 different strategies for the retrieval of aerosol properties. In this sense, we have considered other strategies
631 in this study to choose the one which provides the best results. These strategies are based on the temporal
632 multi-pixel approach offered by GRASP (Lopatin et al., 2021), that constraints the variation of aerosol
633 properties in time, forcing them to vary smoothly. The multi-pixel approach was firstly used in combination
634 with the ‘models’ approach. In order to avoid the problems derived of having fixed aerosol models with
635 fixed aerosol properties, the temporal multi-pixel was also used assuming the size distribution as a bimodal
636 (fine and coarse modes) log-normal distribution and the refractive indices have no dependence on
637 wavelength. None of these methods significantly improved the retrieval of aerosol properties ~~but slightly~~
638 ~~reduce it; likely due to the intrusion of contaminated measurements that influenced the retrieval,~~ but they
639 did reduce the computation time (the data of a full day are inverted all at the same time). Nevertheless,
640 these strategies could be considered for future aerosol retrievals.

641 6. Conclusions

642 This paper has explored the capabilities to calibrate a ZEN-R52 radiometer using the GRASP
643 (Generalized Retrieval of Atmosphere and Surface Properties) code and to retrieve aerosol properties from
644 measured zenith sky radiances (ZSR) at four wavelengths. The ZSR values measured by the ZEN-R52
645 radiometer for solar zenith angle (SZA) values below 30° are contaminated by stray sun light intru-
646 sion and, hence, should not be used. For some latitudes this would result in the absence of measurements for
647 ~~most of the time~~ a substantial amount of time, and therefore a technical improvement in the instrument to
648 correct this issue is recommended to the manufacturers.

649 The proposed methodology for the calibration of ~~then~~ ZEN-R52, using simulated ZSR values has been
650 contrasted, showing discrepancies lower than 6% respect to the calibration coefficients obtained against an
651 integrating sphere. This proposed methodology incorporates the advantage that it includes the
652 normalization used by GRASP, ~~so the need to use an extraterrestrial spectra~~ extraterrestrial spectrum to
653 normalize the data when using it as input to GRASP can be avoided, ~~and therefore there is not any need to~~
654 ~~use extraterrestrial spectra to normalize the data when they are used as input in GRASP.~~

655 A new inversion strategy, called GRASP-ZEN, has been proposed to retrieve aerosol properties with
656 GRASP code using the ZSR values measured by ZEN-R52. An analysis with synthetic data has concluded
657 that ZSR measurements are useful to derive aerosol optical depth (AOD), since these measurements are
658 sensitive to aerosol load and type for the ZEN-R52 channels, at least for AOD at 440 nm below 1 for SZA
659 $\leq 50^{\circ}$. This sensitivity decreases when SZA increases due to the decrease on the intensity of the ZSR values.
660 ~~A couple of tests~~ Two different tests with synthetic data have revealed that the GRASP-ZEN inversion
661 strategy generally overestimates the AOD for all channels under real aerosol scenarios.

662 The GRASP-ZEN method has been applied to ZSR measurements recorded with a ZEN-R52
663 radiometer at Valladolid (Spain) for two years and half. A direct comparison of some retrieved aerosol
664 properties against independent AERONET (Aerosol Robotic Network) products has pointed out the
665 accuracy and precision of the aerosol properties retrieved by GRASP-ZEN. The correlation between the
666 AOD retrieved by GRASP-ZEN and AERONET is high, with determination coefficients (r^2) about 0.86,
667 0.85, 0.79 and 0.72 for 440, 500, 675 and 870 nm, respectively. The uncertainties on the retrieved AOD
668 values are between ± 0.02 and ± 0.03 considering the AERONET values as reference. AERONET offers
669 uncertainties about ± 0.01 for wavelengths above 440 nm, and therefore the uncertainty achieved by the
670 proposed method is higher than the offered by the reference value.

671 With respect other aerosol properties, the GRASP-ZEN retrieval is limited for the intensive properties,
672 like complex refractive index and some size distribution parameters due to the use of the ‘models’ approach
673 of GRASP. Nevertheless, the retrieved volume concentrations, which are extensive properties, have been
674 compared against the same independent AERONET products to quantify the relative accuracy and precision
675 in these concentrations retrieved by GRASP-ZEN. The r^2 obtained comparing the volume concentrations
676 obtained with GRASP-ZEN with respect to the AERONET reference values show low values for the fine
677 (0.57) and coarse (0.56) modes, while for the total volume concentration a higher value (0.66) has been
678 obtained. Nevertheless, the median and standard deviation of the differences on volume concentration
679 between GRASP-ZEN and AERONET are lower than $0.01 \mu\text{m}^3/\mu\text{m}^2$ and $0.02 \mu\text{m}^3/\mu\text{m}^2$, respectively, for
680 ~~both fine and coarse mode and also~~ total concentration. These results have indicated that GRASP-ZEN
681 is capable to retrieve the aerosol volume concentrations with good accuracy and precision.

682 This paper shows the potential of a simple and robust radiometer like the ZEN-R52 as a possible
683 alternative for aerosol properties retrieval in remote areas [or even in places with a collocated CE318](#)
684 [photometer in order to increase the time resolution](#). The proposed methodology would require of a previous
685 coincident period of measurements collocated with an AERONET CE318 photometer to achieve the
686 calibration, and later could be deployed in a remote site in order to broaden the aerosol monitoring network.
687 [This methodology also represents a major advance over the former ZEN-LUT proposed by Almansa et al.](#)
688 [\(2020\) for aerosol properties retrieval, since it is not linked to the place of study](#). This paper also assesses
689 the capability from GRASP to retrieve aerosol properties using only ZSR at 440, 500, 675 and 870 nm. The
690 uncertainty and bias found in the retrieval show the limitations of the instrument and inversion strategy, but
691 also demonstrate that the ZEN-R52, together with the developed GRASP-ZEN strategy, can provide useful
692 information about the AOD and aerosol volume concentration for total, fine and coarse modes. [This can be](#)
693 [especially useful for remote areas or even in places with collocated a CE318 photometer in order to increase](#)
694 [the time resolution](#).
695
696

697 **Acknowledgments**

698 This research has been supported by the Ministerio de Ciencia e Innovación (grant no. PID2021-
699 127588OB-I00), the Junta de Castilla y León (grant no. VA227P20). This publication is part of the
700 TED2021-131211B-I00 project funded by MCIN/AEI/10.13039/501100011033 and European Union
701 “NextGenerationEU”/PRTR. This article is based upon work from COST Action CA21119 HARMONIA,
702 supported by COST (European Cooperation in Science and Technology) and has been supported by the
703 European Metrology Program for Innovation and Research (EMPIR) within the joint research project
704 EMPIR 19ENV04 MAPP. We especially thank the GOA-UVa staff members (Rogelio Carracedo, Patricia
705 Martín-Sánchez and Javier Gatón), for helping with the research through the maintenance of the instruments
706 and the station infrastructure.

707 **References**

- 708 Almansa, A. F., Cuevas, E., Barreto, Á., Torres, B., García, O. E., García, R. D., Velasco-Merino, C.,
709 Cachorro, V. E., Berjón, A., Mallorquín, M., López, C., Ramos, R., Guirado-Fuentes, C., Negrillo,
710 R., & de Frutos, Á. M. (2020). Column integrated water vapor and aerosol load characterization
711 with the new ZEN-R52 radiometer. *Remote Sensing*, 12(9). <https://doi.org/10.3390/RS12091424>
- 712 Almansa, A. F., Cuevas, E., Torres, B., Barreto, Á., García, R. D., Cachorro, V. E., De Frutos, Á. M.,
713 López, C., & Ramos, R. (2017). A new zenith-looking narrow-band radiometer-based system
714 (ZEN) for dust aerosol optical depth monitoring. *Atmospheric Measurement Techniques*, 10(2),
715 565–579. <https://doi.org/10.5194/AMT-10-565-2017>
- 716 Ångström, A. (1964). The parameters of atmospheric turbidity. *Tellus*, 16(1), 64–75.
717 <https://doi.org/10.1111/J.2153-3490.1964.TB00144.X>
- 718 Barker, H. W., & Marshak, A. (2001). Inferring Optical Depth of Broken Clouds above Green Vegetation
719 Using Surface Solar Radiometric Measurements. *Journal of the Atmospheric Sciences*, 58(20),
720 2989–3006. [https://doi.org/10.1175/1520-0469\(2001\)058<2989:IODOBC>2.0.CO;2](https://doi.org/10.1175/1520-0469(2001)058<2989:IODOBC>2.0.CO;2)
- 721 Barreto, Á., Cuevas, E., Granados-Muñoz, M. J., Alados-Arboledas, L., Romero, P. M., Gröbner, J.,
722 Kouremeti, N., Almansa, A. F., Stone, T., Toledano, C., Román, R., Sorokin, M., Holben, B.,
723 Canini, M., & Yela, M. (2016). The new sun-sky-lunar Cimel CE318-T multiband photometer
724 – A comprehensive performance evaluation. *Atmospheric Measurement Techniques*, 9(2),
725 631–654. <https://doi.org/10.5194/AMT-9-631-2016>
- 726 Barreto, A., Román, R., Cuevas, E., Pérez-Ramírez, D., Berjón, A. J., Kouremeti, N., Kazadzis, S.,
727 Gröbner, J., Mazzola, M., Toledano, C., Benavent-Oltra, J. A., Doppler, L., Juryšek, J., Almansa,
728 A. F., Victori, S., Maupin, F., Guirado-Fuentes, C., González, R., Vitale, V., ... Yela, M. (2019).
729 Evaluation of night-time aerosols measurements and lunar irradiance models in the frame of the
730 first multi-instrument nocturnal intercomparison campaign. *Atmospheric Environment*, 202, 190–
731 211. <https://doi.org/10.1016/J.ATMOENV.2019.01.006>
- 732 Benavent-Oltra, J. A., Román, R., Andrés Casquero-Vera, J., Pérez-Ramírez, D., Lyamani, H., Ortiz-
733 Amezcua, P., Bedoya-Velásquez, A. E., De Arruda Moreira, G., Barreto, Á., Lopatin, A., Fuertes,
734 D., Herrera, M., Torres, B., Dubovik, O., Luis Guerrero-Rascado, J., Goloub, P., Olmo-Reyes, F. J.,
735 & Alados-Arboledas, L. (2019). Different strategies to retrieve aerosol properties at night-time with
736 the GRASP algorithm. *Atmospheric Chemistry and Physics*, 19(22), 14149–14171.
737 <https://doi.org/10.5194/ACP-19-14149-2019>
- 738 Benavent-Oltra, J. A., Román, R., Granados-Munõz, M. J., Pérez-Ramírez, D., Ortiz-Amezcua, P.,
739 Denjean, C., Lopatin, A., Lyamani, H., Torres, B., Guerrero-Rascado, J. L., Fuertes, D., Dubovik,
740 O., Chaikovsky, A., Olmo, F. J., Mallet, M., & Alados-Arboledas, L. (2017). Comparative
741 assessment of GRASP algorithm for a dust event over Granada (Spain) during ChArMEx-
742 ADRIMED 2013 campaign. *Atmospheric Measurement Techniques*, 10(11), 4439–4457.
743 <https://doi.org/10.5194/AMT-10-4439-2017>
- 744 Bennouna, Y. S., Cachorro, V. E., Torres, B., Toledano, C., Berjón, A., de Frutos, A. M., & Alonso
745 Fernández Coppel, I. (2013). Atmospheric turbidity determined by the annual cycle of the aerosol

- 746 optical depth over north-center Spain from ground (AERONET) and satellite (MODIS).
747 Atmospheric Environment, 67, 352–364. <https://doi.org/10.1016/J.ATMOSENV.2012.10.065>
- 748 Boucher, O., Randall, D., Artaxo, P., Bretherton, C., Feingold, G., Forster, P., Kerminen, V., Kondo, Y.,
749 Liao, H., Lohmann, U., Rasch, P., Satheesh, S., Sherwood, S., Stevens, B., & Zhang, X. (2013).
750 Clouds and Aerosols. In: Climate Change 2013: The Physical Science Basis. Contribution of
751 Working Group I to the Fifth Assessment Report of the Intergovernmental Panel on Climate
752 Change Coordinating Lead Authors: Lead Authors.
753 <https://doi.org/10.1017/CBO9781107415324.016>
- 754 Cachorro, V. E., Burgos, M. A., Mateos, D., Toledano, C., Bennouna, Y., Torres, B., De Frutos, Á. M., &
755 Herguedas, Á. (2016). Inventory of African desert dust events in the north-central Iberian Peninsula
756 in 2003-2014 based on sun-photometer-AERONET and particulate-mass-EMEP data. Atmospheric
757 Chemistry and Physics, 16(13), 8227–8248. <https://doi.org/10.5194/ACP-16-8227-2016>
- 758 Chen, C., Dubovik, O., Fuertes, D., Litvinov, P., Lapyonok, T., Lopatin, A., Ducos, F., Derimian, Y.,
759 Herman, M., Tanré, D., Remer, L. A., Lyapustin, A., Sayer, A. M., Levy, R. C., Christina Hsu, N.,
760 Descloitres, J., Li, L., Torres, B., Karol, Y., ... Federspiel, C. (2020). Validation of GRASP
761 algorithm product from POLDER/PARASOL data and assessment of multi-angular polarimetry
762 potential for aerosol monitoring. Earth System Science Data, 12(4), 3573–3620.
763 <https://doi.org/10.5194/ESSD-12-3573-2020>
- 764 Chiu, C. J., Huang, C.-H., Marshak, A., Slutsker, I., Giles, D. M., Holben, B. N., Knyazikhin, Y.,
765 Wiscombe, W. J., Huang, C., Marshak, A., Slutsker, I., Giles, D. M., Holben, B. N., Knyazikhin,
766 Y., & Wiscombe, W. J. (2010). Cloud optical depth retrievals from the Aerosol Robotic Network
767 (AERONET) cloud mode observations. Journal of Geophysical Research: Atmospheres, 115(D14),
768 14202. <https://doi.org/10.1029/2009JD013121>
- 769 [Cissé, G., McLeman, R., Adams, H., Aldunce, P., Bowen, K., Campbell-Lendrum, D., Clayton, S., Ebi,
770 K. L., Hess, J., Huang, C., Liu, Q., McGregor, G., Semenza, J., & Tirado, M. C. \(2022\). Health,
771 Wellbeing, and the Changing Structure of Communities. In: Climate Change 2022: Impacts,
772 Adaptation, and Vulnerability. Contribution of Working Group II to the Sixth Assessment Report of
773 the Intergovernmental Panel on Climate Change \[H. O. Pörtner, D.C. Roberts, M. Tignor, E.S.
774 Poloczanska, K. Mintenbeck, A. Alegría, M. Craig, S. Langsdorf, S. Löschke, V. Möller, A. Okem,
775 B. Rama \(eds.\)\]. <https://doi.org/10.1017/9781009325844.008>.](https://doi.org/10.1017/9781009325844.008)
- 776 Dubovik, O., Fuertes, D., Litvinov, P., Lopatin, A., Lapyonok, T., Dubovik, I., Xu, F., Ducos, F., Chen,
777 C., Torres, B., Derimian, Y., Li, L., Herreras-Giralda, M., Herrera, M., Karol, Y., Matar, C.,
778 Schuster, G. L., Espinosa, R., Puthukkudy, A., ... Federspiel, C. (2021). A Comprehensive
779 Description of Multi-Term LSM for Applying Multiple a Priori Constraints in Problems of
780 Atmospheric Remote Sensing: GRASP Algorithm, Concept, and Applications. Frontiers in Remote
781 Sensing, 2, 23. <https://doi.org/10.3389/FRSEN.2021.706851>
- 782 Dubovik, O., & King, M. D. (2000). A flexible inversion algorithm for retrieval of aerosol optical
783 properties from Sun and sky radiance measurements. Journal of Geophysical Research:
784 Atmospheres, 105(D16), 20673–20696. <https://doi.org/10.1029/2000JD900282>
- 785 Dubovik, O., Lapyonok, T., Litvinov, P., Herman, M., Fuertes, D., Ducos, F., Torres, B., Derimian, Y.,
786 Huang, X., Lopatin, A., Chaikovskiy, A., Aspetsberger, M., & Federspiel, C. (2014). GRASP: a
787 versatile algorithm for characterizing the atmosphere. SPIE Newsroom.
788 <https://doi.org/10.1117/2.1201408.005558>
- 789 Eilers, P. H. C., & Goeman, J. J. (2004). Enhancing scatterplots with smoothed densities. Bioinformatics,
790 20(5), 623–628. <https://doi.org/10.1093/BIOINFORMATICS/BTG454>
- 791 Espinosa, W. R., Remer, L. A., Dubovik, O., Ziemba, L., Beyersdorf, A., Orozco, D., Schuster, G.,
792 Lapyonok, T., Fuertes, D., & Vanderlei Martins, J. (2017). Retrievals of aerosol optical and
793 microphysical properties from Imaging Polar Nephelometer scattering measurements. Atmospheric
794 Measurement Techniques, 10(3), 811–824. <https://doi.org/10.5194/AMT-10-811-2017>

- 795 [Forster, P., T. Storelvmo, K. Armour, W. Collins, J.-L. Dufresne, D. Frame, D.J. Lunt, T. Mauritsen,](#)
796 [M.D. Palmer, M. Watanabe, M. Wild, and H. Zhang, 2021: The Earth's Energy Budget, Climate](#)
797 [Feedbacks, and Climate Sensitivity. In *Climate Change 2021: The Physical Science Basis.*](#)
798 [Contribution of Working Group I to the Sixth Assessment Report of the Intergovernmental Panel on](#)
799 [Climate Change \[Masson-Delmotte, V., P. Zhai, A. Pirani, S.L. Connors, C. Péan, S. Berger, N.](#)
800 [Caud, Y. Chen, L. Goldfarb, M.I. Gomis, M. Huang, K. Leitzell, E. Lonnoy, J.B.R. Matthews, T.K.](#)
801 [Maycock, T. Waterfield, O. Yelekçi, R. Yu, and B. Zhou \(eds.\)\]. Cambridge University Press,](#)
802 [Cambridge, United Kingdom and New York, NY, USA, pp. 923–1054.](#)
803 <https://doi.org/10.1017/9781009157896.009>
- 804 Fuertes, D., Toledano, C., González, R., Berjón, A., Torres, B., Cachorro, V. E., & De Frutos, Á. M.
805 (2018). CÆLIS: Software for assimilation, management and processing data of an atmospheric
806 measurement network. *Geoscientific Instrumentation, Methods and Data Systems*, 7(1), 67–81.
807 <https://doi.org/10.5194/GI-7-67-2018>
- 808 Giles, D. M., Sinyuk, A., Sorokin, M. G., Schafer, J. S., Smirnov, A., Slutsker, I., Eck, T. F., Holben, B.
809 N., Lewis, J. R., Campbell, J. R., Welton, E. J., Korkin, S. V., & Lyapustin, A. I. (2019).
810 Advancements in the Aerosol Robotic Network (AERONET) Version 3 database - Automated near-
811 real-time quality control algorithm with improved cloud screening for Sun photometer aerosol
812 optical depth (AOD) measurements. *Atmospheric Measurement Techniques*, 12(1), 169–209.
813 <https://doi.org/10.5194/AMT-12-169-2019>
- 814 González, R., Toledano, C., Román, R., Fuertes, D., Berjón, A., Mateos, D., Guirado-Fuentes, C.,
815 Velasco-Merino, C., Antuña-Sánchez, J. C., Calle, A., Cachorro, V. E., & De Frutos, Á. M. (2020).
816 Daytime and nighttime aerosol optical depth implementation in CÆLIS. *Geoscientific*
817 *Instrumentation, Methods and Data Systems*, 9(2), 417–433. <https://doi.org/10.5194/GI-9-417-2020>
- 818 Herreras, M., Román, R., Cazorla, A., Toledano, C., Lyamani, H., Torres, B., Cachorro, V. E., Olmo, F.
819 J., Alados-Arboledas, L., & de Frutos, A. M. (2019). Evaluation of retrieved aerosol extinction
820 profiles using as reference the aerosol optical depth differences between various heights.
821 *Atmospheric Research*, 230, 104625. <https://doi.org/10.1016/J.ATMOSRES.2019.104625>
- 822 Herreras-Giralda, M., Litvinov, P., Dubovik, O., Derimian, Y., Lapyonok, T., Fuertes, D., Sourdeval, O.,
823 Preusker, R., & Fischer, J. (2022). Thermal emission in the successive orders of scattering (SOS)
824 radiative transfer approach. *Journal of Quantitative Spectroscopy and Radiative Transfer*, 291,
825 108327. <https://doi.org/10.1016/J.JQSRT.2022.108327>
- 826 Holben, B. N., Eck, T. F., Slutsker, I., Tanré, D., Buis, J. P., Setzer, A., Vermote, E., Reagan, J. A.,
827 Kaufman, Y. J., Nakajima, T., Lavenu, F., Jankowiak, I., & Smirnov, A. (1998). AERONET—A
828 Federated Instrument Network and Data Archive for Aerosol Characterization. *Remote Sensing of*
829 *Environment*, 66(1), 1–16. [https://doi.org/10.1016/S0034-4257\(98\)00031-5](https://doi.org/10.1016/S0034-4257(98)00031-5)
- 830 Lenoble, J., Herman, M., Deuzé, J. L., Lafrance, B., Santer, R., & Tanré, D. (2007). A successive order of
831 scattering code for solving the vector equation of transfer in the earth's atmosphere with aerosols.
832 *Journal of Quantitative Spectroscopy and Radiative Transfer*, 107(3), 479–507.
833 <https://doi.org/10.1016/J.JQSRT.2007.03.010>
- 834 Lopatin, A., Dubovik, O., Chaikovskiy, A., Goloub, P., Lapyonok, T., Tanré, D., & Litvinov, P. (2013).
835 Enhancement of aerosol characterization using synergy of lidar and sun-photometer coincident
836 observations: The GARRLiC algorithm. *Atmospheric Measurement Techniques*, 6(8), 2065–2088.
837 <https://doi.org/10.5194/AMT-6-2065-2013>
- 838 Lopatin, A., Dubovik, O., Fuertes, D., Stenchikov, G., Lapyonok, T., Veselovskii, I., Wienhold, F. G.,
839 Shevchenko, I., Hu, Q., & Parajuli, S. (2021). Synergy processing of diverse ground-based remote
840 sensing and in situ data using the GRASP algorithm: applications to radiometer, lidar and
841 radiosonde observations. *Atmospheric Measurement Techniques*, 14(3), 2575–2614.
842 <https://doi.org/10.5194/AMT-14-2575-2021>

- 843 Marshak, A., Knyazikhin, Y., Davis, A. B., Wiscombe, W. J., & Pilewskie, P. (2000). Cloud-vegetation
844 interaction: Use of normalized difference cloud index for estimation of cloud optical thickness.
845 *Geophysical Research Letters*, 27(12), 1695–1698. <https://doi.org/10.1029/1999GL010993>
- 846 Mateos, D., Cachorro, V. E., Velasco-Merino, C., O'Neill, N. T., Burgos, M. A., Gonzalez, R., Toledano,
847 C., Herreras, M., Calle, A., & de Frutos, A. M. (2020). Comparison of three different
848 methodologies for the identification of high atmospheric turbidity episodes. *Atmospheric Research*,
849 237, 104835. <https://doi.org/10.1016/j.atmosres.2019.104835>
- 850 Molero, F., Pujadas, M., & Artíñano, B. (2020). Study of the Effect of Aerosol Vertical Profile on
851 Microphysical Properties Using GRASP Code with Sun/Sky Photometer and Multiwavelength
852 Lidar Measurements. *Remote Sensing 2020*, Vol. 12, Page 4072, 12(24), 4072.
853 <https://doi.org/10.3390/RS12244072>
- 854 Myhre, G., Shindell, D., Bréon, F., Collins, W., Fuglestvedt, J., Huang, J., Koch, D., Lamarque, J., Lee,
855 D., Mendoza, B., Nakajima, T., Robock, A., Stephens, G., Takemura, T., & Zhang, H. (2013).
856 Anthropogenic and Natural Radiative Forcing. In: *Climate Change 2013: The Physical Science*
857 *Basis. Contribution of Working Group I*. <https://doi.org/10.1017/CBO9781107415324.018>
- 858 Nakajima, T., Tonna Glauco, Rao, R., Boi, P., Kaufman, Y., & Holben, B. (1996). Use of sky brightness
859 measurements from ground for remote sensing of particulate polydispersions. *Applied Optics*, Vol.
860 35, Issue 15, Pp. 2672–2686, 35(15), 2672–2686. <https://doi.org/10.1364/AO.35.002672>
- 861 Román, R., Antuña-Sánchez, J. C., Cachorro, V. E., Toledano, C., Torres, B., Mateos, D., Fuertes, D.,
862 López, C., González, R., Lapionok, T., Herreras-Giralda, M., Dubovik, O., & De Frutos, Á. M.
863 (2022). Retrieval of aerosol properties using relative radiance measurements from an all-sky
864 camera. *Atmospheric Measurement Techniques*, 15(2), 407–433. [https://doi.org/10.5194/AMT-15-](https://doi.org/10.5194/AMT-15-407-2022)
865 [407-2022](https://doi.org/10.5194/AMT-15-407-2022)
- 866 Román, R., Benavent-Oltra, J. A., Casquero-Vera, J. A., Lopatin, A., Cazorla, A., Lyamani, H., Denjean,
867 C., Fuertes, D., Pérez-Ramírez, D., Torres, B., Toledano, C., Dubovik, O., Cachorro, V. E., de
868 Frutos, A. M., Olmo, F. J., & Alados-Arboledas, L. (2018). Retrieval of aerosol profiles combining
869 sunphotometer and ceilometer measurements in GRASP code. *Atmospheric Research*, 204, 161–
870 177. <https://doi.org/10.1016/J.ATMOSRES.2018.01.021>
- 871 Román, R., Bilbao, J., & de Miguel, A. (2014). Reconstruction of six decades of daily total solar
872 shortwave irradiation in the Iberian Peninsula using sunshine duration records. *Atmospheric*
873 *Environment*, 99, 41–50. <https://doi.org/10.1016/J.ATMOSENV.2014.09.052>
- 874 Román, R., González, R., Toledano, C., Barreto, Á., Pérez-Ramírez, D., Benavent-Oltra, J. A., Olmo, F.
875 J., Cachorro, V. E., Alados-Arboledas, L., & de Frutos, Á. M. (2020). Correction of a lunar-
876 irradiance model for aerosol optical depth retrieval and comparison with a star photometer.
877 *Atmospheric Measurement Techniques*, 13(11), 6293–6310. [https://doi.org/10.5194/AMT-13-6293-](https://doi.org/10.5194/AMT-13-6293-2020)
878 [2020](https://doi.org/10.5194/AMT-13-6293-2020)
- 879 Román, R., Torres, B., Fuertes, D., Cachorro, V. E., Dubovik, O., Toledano, C., Cazorla, A., Barreto, A.,
880 Bosch, J. L., Lapyonok, T., González, R., Goloub, P., Perrone, M. R., Olmo, F. J., de Frutos, A., &
881 Alados-Arboledas, L. (2017). Remote sensing of lunar aureole with a sky camera: Adding
882 information in the nocturnal retrieval of aerosol properties with GRASP code. *Remote Sensing of*
883 *Environment*, 196, 238–252. <https://doi.org/10.1016/J.RSE.2017.05.013>
- 884 Schaaf, C., Liu, J., Gao, F., & Strahler, A. H. (2011). MODIS albedo and reflectance anisotropy products
885 from Aqua and Terra, *Land Remote Sensing and Global Environmental Change: NASA's Earth*
886 *Observing System and the Science of ASTER and MODIS*. 11, 549–561.
- 887 Sinyuk, A., Sinyuk, A., Holben, B. N., Eck, T. F., Eck, T. F., M. Giles, D., M. Giles, D., Slutsker, I.,
888 Slutsker, I., Korkin, S., Korkin, S., S. Schafer, J., S. Schafer, J., Smirnov, A., Smirnov, A., Sorokin,
889 M., Sorokin, M., & Lyapustin, A. (2020). The AERONET Version 3 aerosol retrieval algorithm,
890 associated uncertainties and comparisons to Version 2. *Atmospheric Measurement Techniques*,
891 13(6), 3375–3411. <https://doi.org/10.5194/AMT-13-3375-2020>

892 Titos, G., Ealo, M., Román, R., Cazorla, A., Sola, Y., Dubovik, O., Alastuey, A., & Pandolfi, M. (2019).
893 Retrieval of aerosol properties from ceilometer and photometer measurements: Long-term
894 evaluation with in situ data and statistical analysis at Montsec (southern Pyrenees). *Atmospheric
895 Measurement Techniques*, 12(6), 3255–3267. <https://doi.org/10.5194/AMT-12-3255-2019>

896 Torres, B., Dubovik, O., Fuertes, D., Schuster, G., Eugenia Cachorro, V., Lapyonok, T., Goloub, P.,
897 Blarel, L., Barreto, A., Mallet, M., Toledano, C., & Tanré, D. (2017). Advanced characterisation of
898 aerosol size properties from measurements of spectral optical depth using the GRASP algorithm.
899 *Atmospheric Measurement Techniques*, 10(10), 3743–3781. [https://doi.org/10.5194/AMT-10-3743-
2017](https://doi.org/10.5194/AMT-10-3743-

900 2017)

901 Tsekeri, A., Lopatin, A., Amiridis, V., Marinou, E., Igloffstein, J., Siomos, N., Solomos, S., Kokkalis, P.,
902 Engelmann, R., Baars, H., Gratsea, M., Raptis, P. I., Biniatoglou, I., Mihalopoulos, N., Kalivitis, N.,
903 Kouvarakis, G., Bartsotas, N., Kallos, G., Basart, S., ... Dubovik, O. (2017). GARRLiC and LIRIC:
904 strengths and limitations for the characterization of dust and marine particles along with their
905 mixtures. *Atmospheric Measurement Techniques*, 10(12), 4995–5016.
906 <https://doi.org/10.5194/AMT-10-4995-2017>

907 Walker, J. H., Cromer, C. L., & McLean, J. T. (1991). Calibration of passive remote observing optical
908 and microwave instrumentation. *Proc. SPIE—The International Soc. of Optical Engineering*, 3–5
909 April, Orlando, FL, 1493, 224–230.

910 Wei, Y., Li, Z., Zhang, Y., Chen, C., Xie, Y., Lv, Y., & Dubovik, O. (2021). Derivation of PM10 mass
911 concentration from advanced satellite retrieval products based on a semi-empirical physical
912 approach. *Remote Sensing of Environment*, 256, 112319.
913 <https://doi.org/10.1016/J.RSE.2021.112319>

914

915 **List of Tables**

916 **Table 1.** Calibration coefficients obtained using simulations of zenith sky radiance (Coef-SIM) and the
917 ones obtained at the IARC against a calibrated integrating sphere (Coef-IARC). The relative difference (Δ)
918 between both coefficients is included assuming Coef-IARC as reference.

λ (nm)	Coef – SIM (W/m ² nmsr)	Coef- IARC (W/m ² nmsr)	Δ (%)
440	3.2928e-05	3.2485e-05	1.39
500	1.1426e-05	1.2223e-05	-6.54
675	2.0734e-05	2.2221e-05	-6.72
870	1.6840e-05	1.7901e-05	-5.89

919

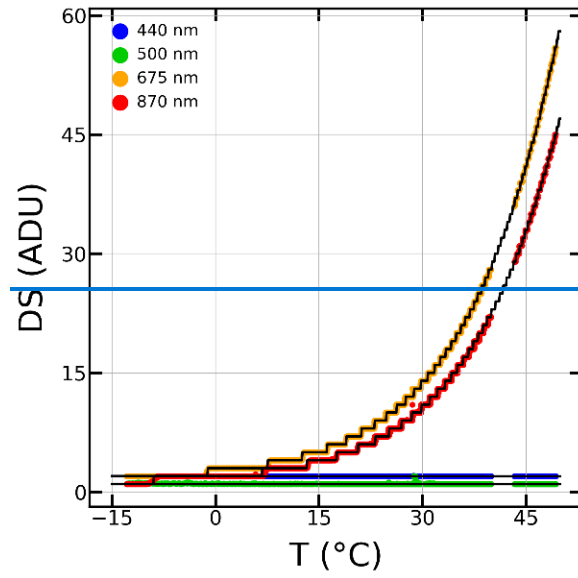
920 **Table 2.** Determination coefficient (r^2) between ZSR_{ZEN} and ZSR_{PPL} and the mean (MBE), median (Md)
921 and standard deviation (SD) of the Δ differences between ZSR_{ZEN} and ZSR_{PPL} at 440nm, 500nm, 675 nm
922 and 870 nm using the calibration coefficient obtained in this paper with simulated ZSR values and the ones
923 obtained with an integrating sphere at IARC in parenthesis. N represents the number of coincident ZSR_{ZEN}
924 and ZSR_{PPL} data pairs.

	λ (nm)	r^2	MBE (%)	SD (%)	Md (%)	N
This paper (IARC)	440	0.99 (0.99)	1.96 (0.73)	3.00 (2.95)	1.36 (0.16)	1327
	500	0.99 (0.99)	-0.34 (6.67)	4.62 (4.95)	-1.39 (5.56)	1317
	675	0.95 (0.95)	3.76 (14.67)	12.54 (13.92)	-0.22 (10.96)	1289
	870	0.94 (0.94)	10.56 (26.67)	21.37 (25.13)	4.99 (20.96)	1165

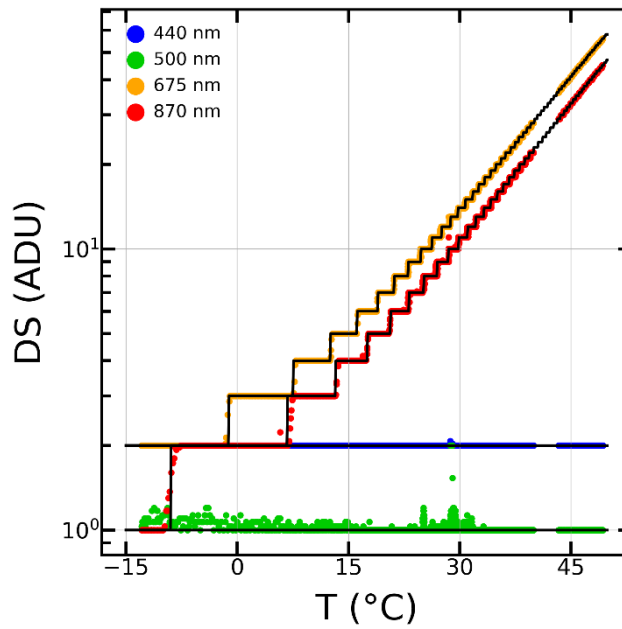
925

926

928

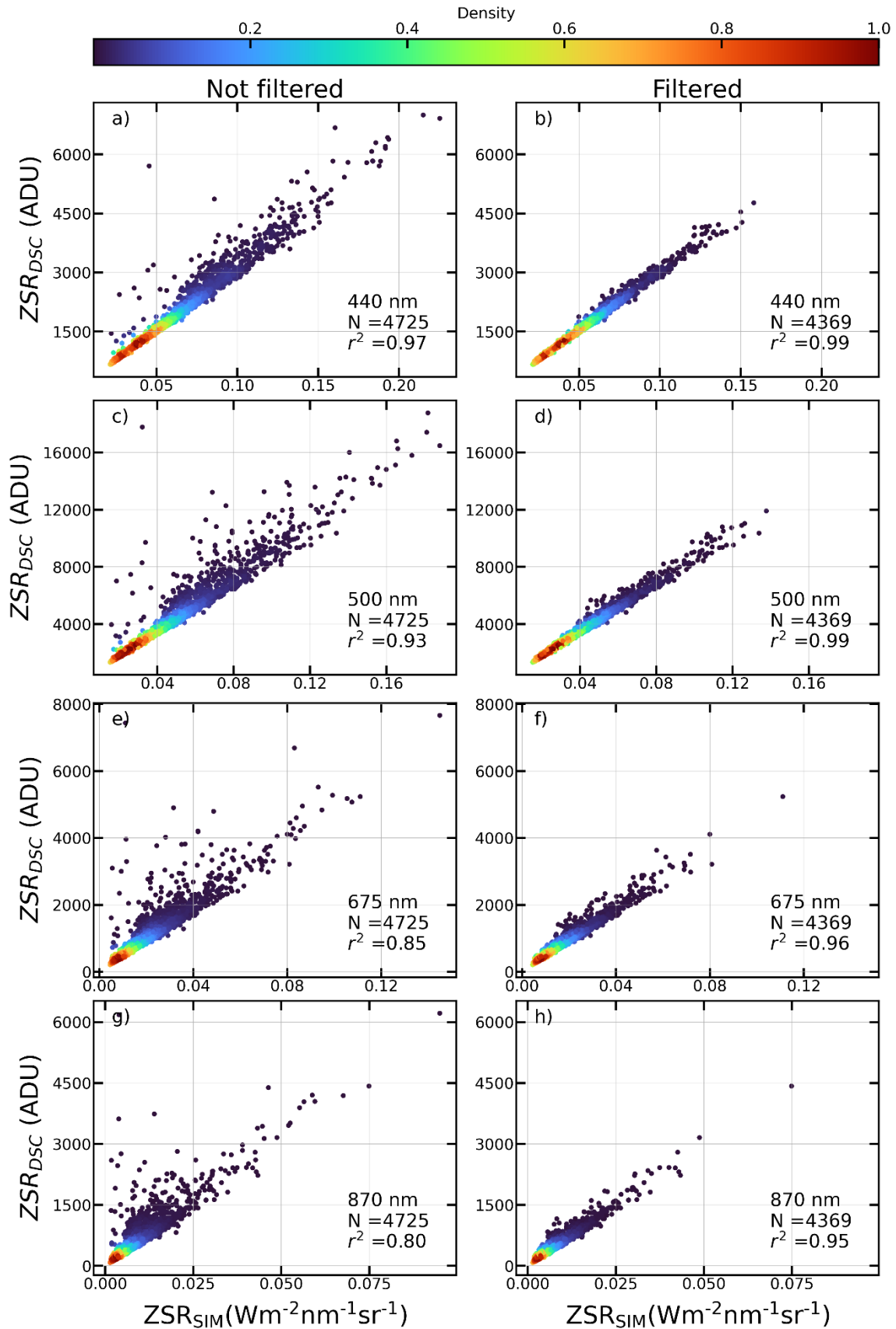


929



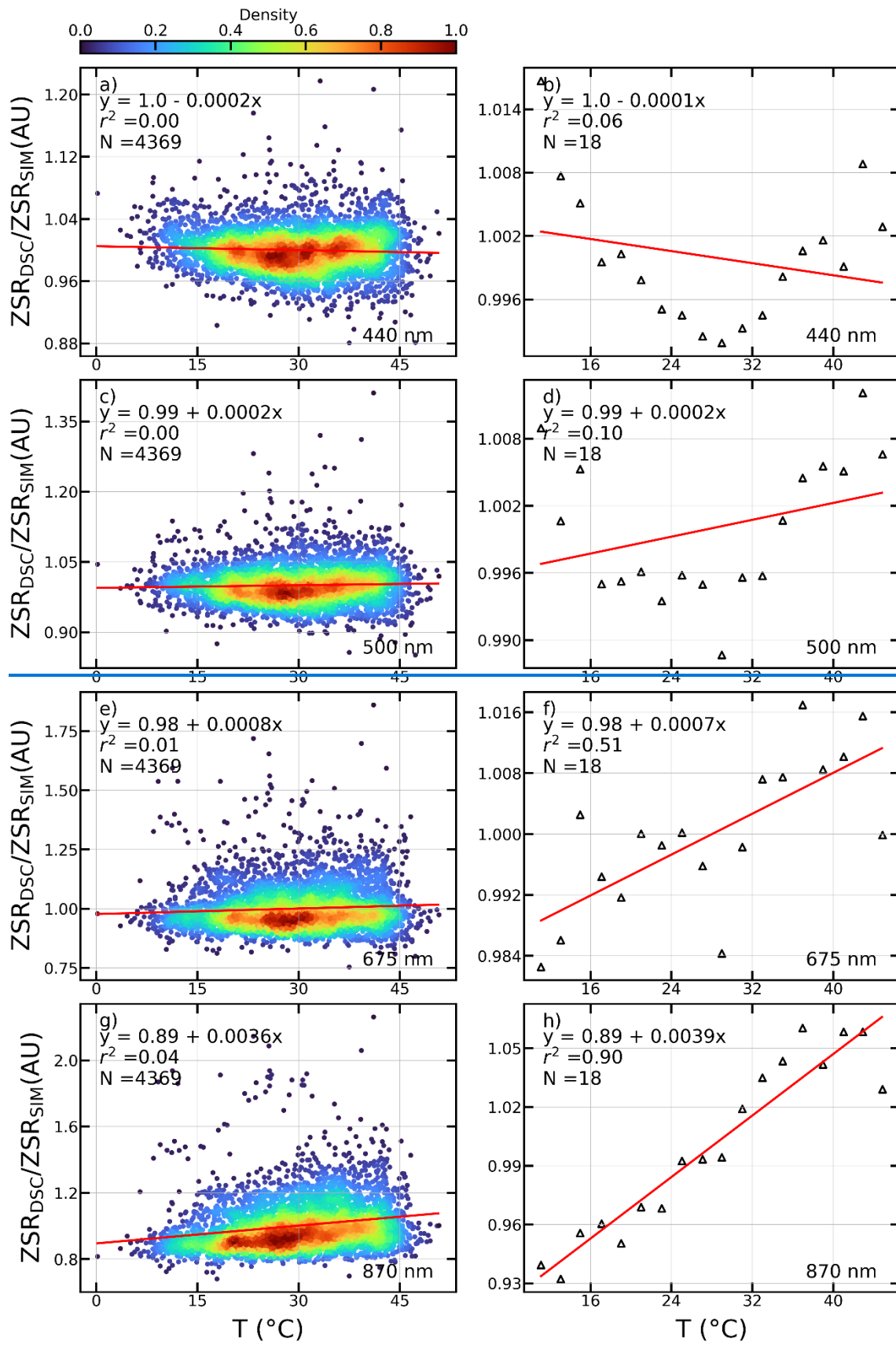
930

931 Figure 1. ZEN-R52 dark signal (DS) in analogic-to-digital units (ADU) against the temperature (coloured dots)
932 at 440, 500, 675 and 870 nm. Black lines represent the DS for each channel.

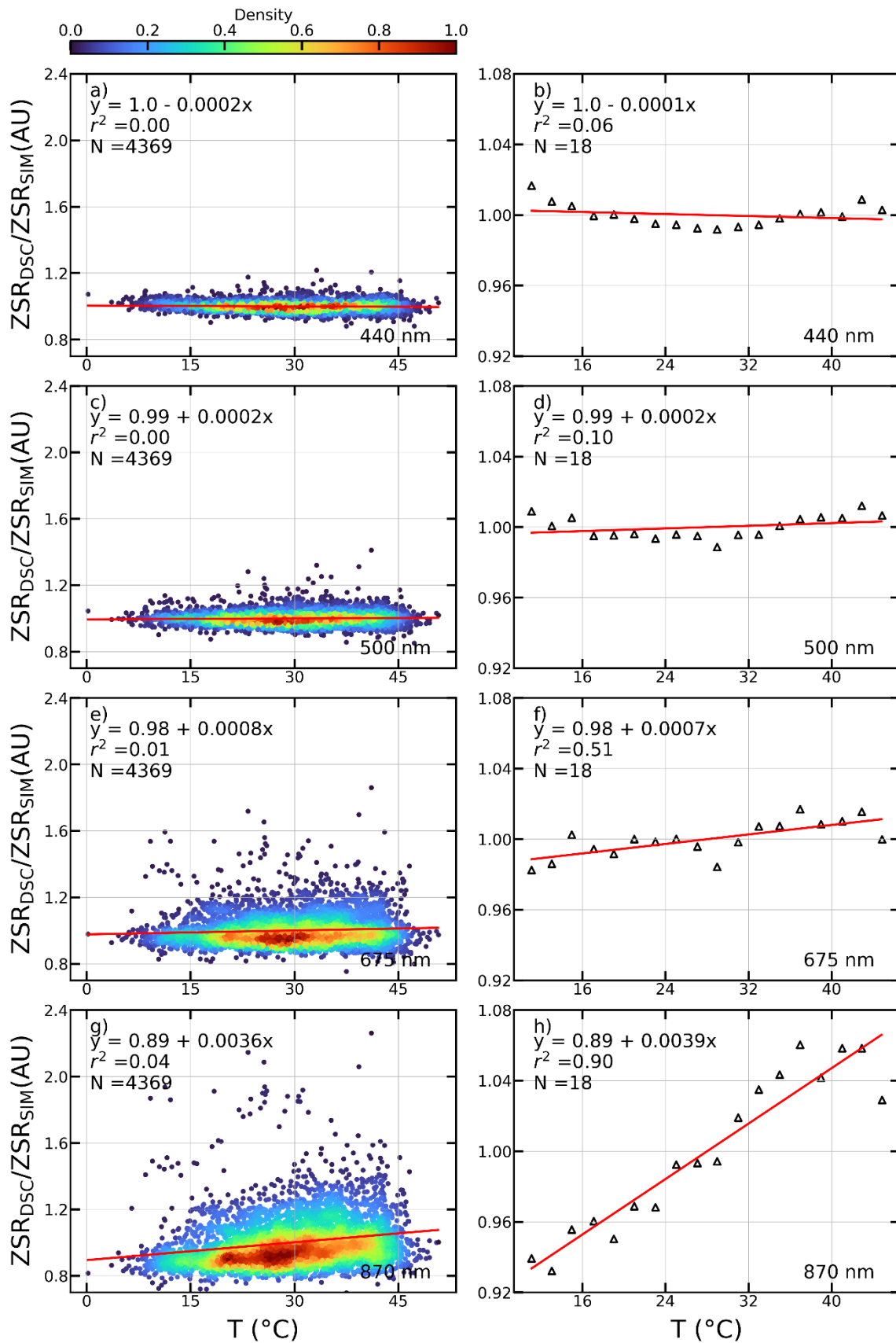


933
934
935
936
937
938

Figure 2. Density scatter plot of the measured zenith sky radiances corrected from dark signal (ZSR_{DSC}), in analogic-to-digital units (ADU), against the zenith sky radiances simulated by GRASP (ZSR_{SIM}), both at 440 nm (upper panels), 500 nm (second row panels), 675 nm (third row panels) and 870 nm (bottom panels). Left and right panels show these data before and after applying a quality control filtering, respectively. Determination coefficient (r^2) and number of data pairs (N) are also shown.



939



940

941

942

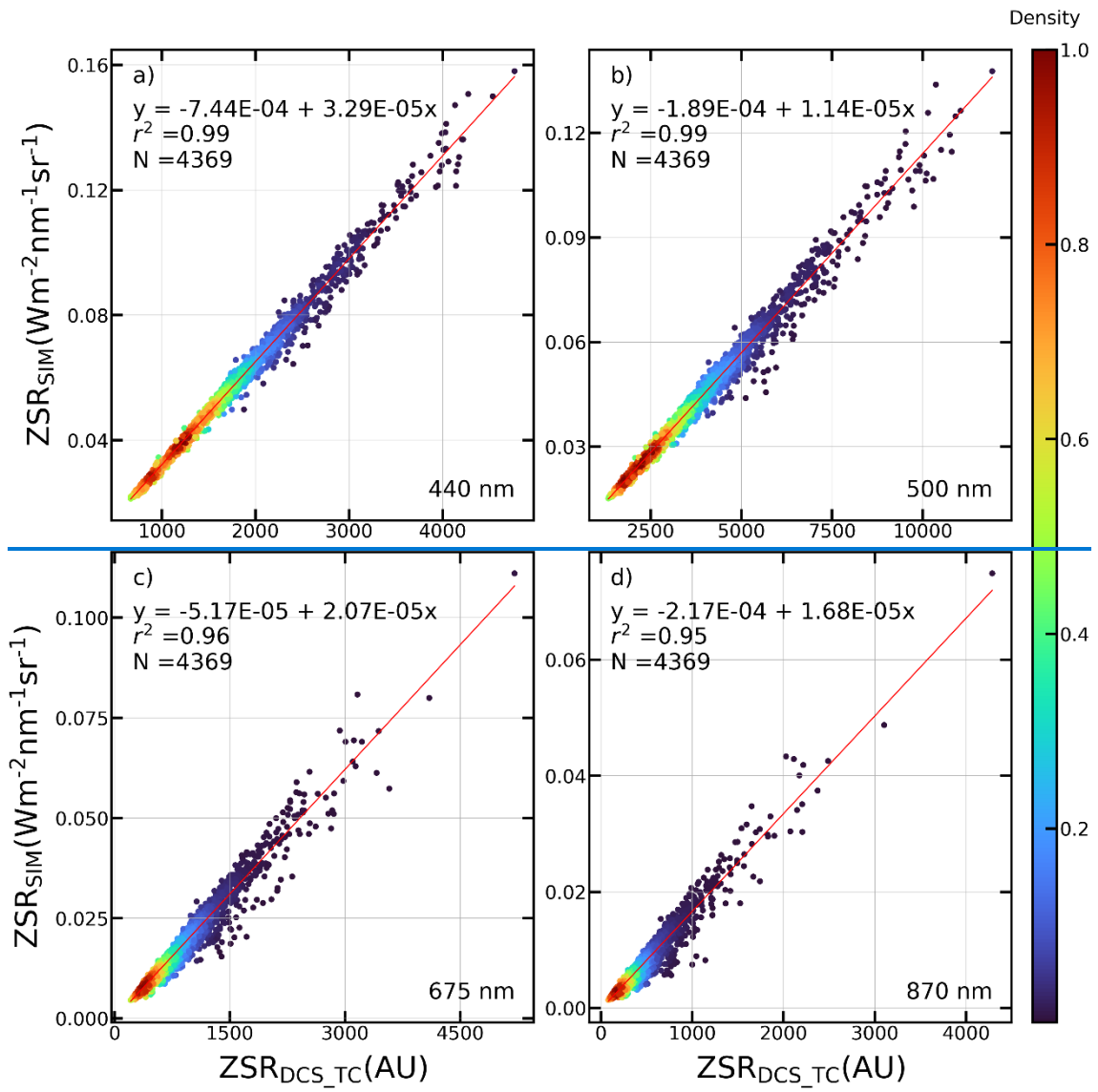
943

944

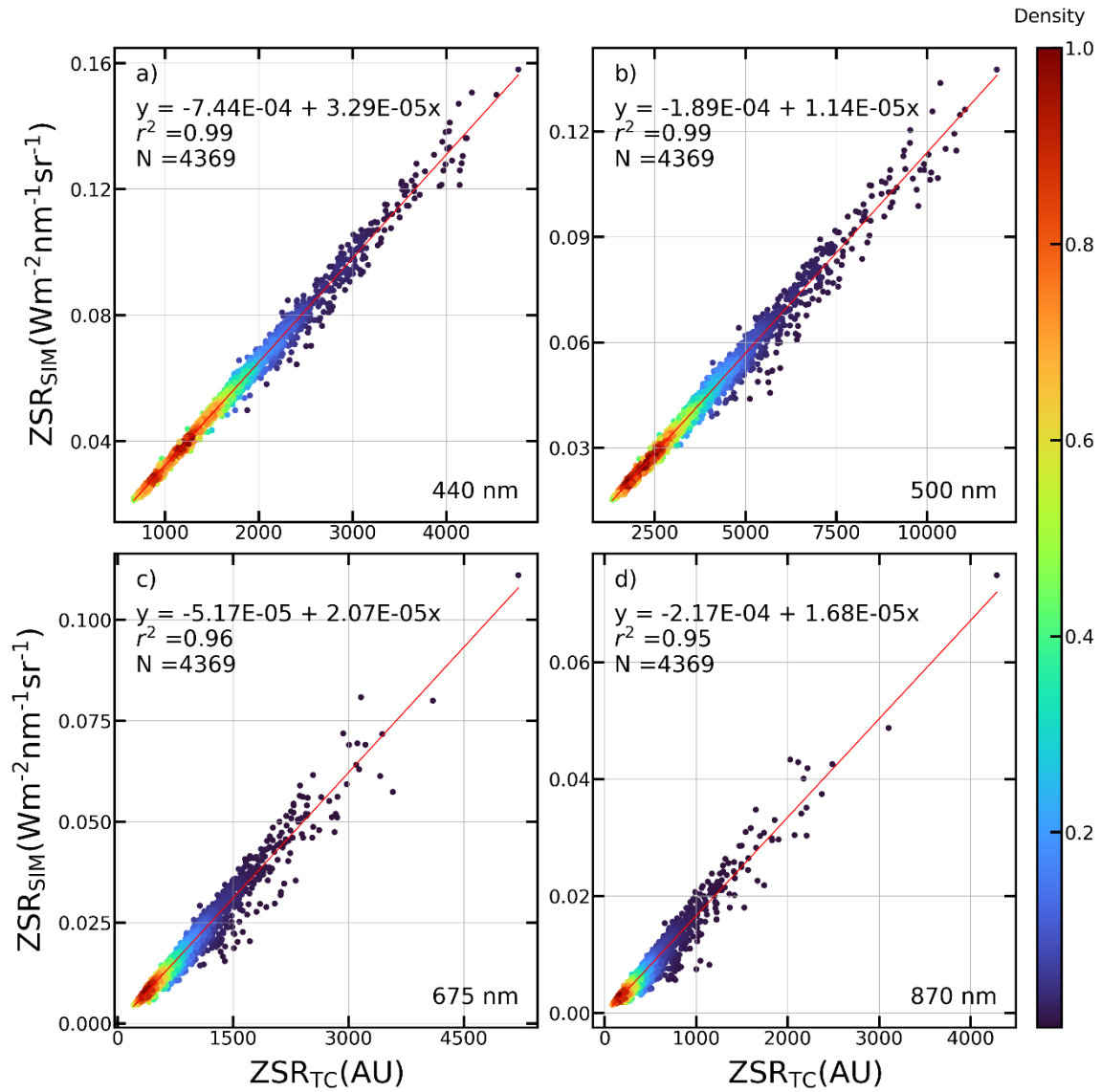
Figure 3. Left panel. density scatter plots for the normalized ratios ZSR_{DSC}/ZSR_{SIM} in arbitrary units (AU) against the temperature at a) 440nm, c) 500nm, e) 675 nm and g) 870 nm. Right panel. scatter plot of the median value for the ratios ZSR_{DSC}/ZSR_{SIM} grouped in 2°C ranges against mean temperature of the group at b) 440nm,

945 d) 500nm, f) 675 nm and h) 870 nm. Linear fit (red line), determination coefficient (r^2) and its equation and
946 number of data points (N) are also shown.

947

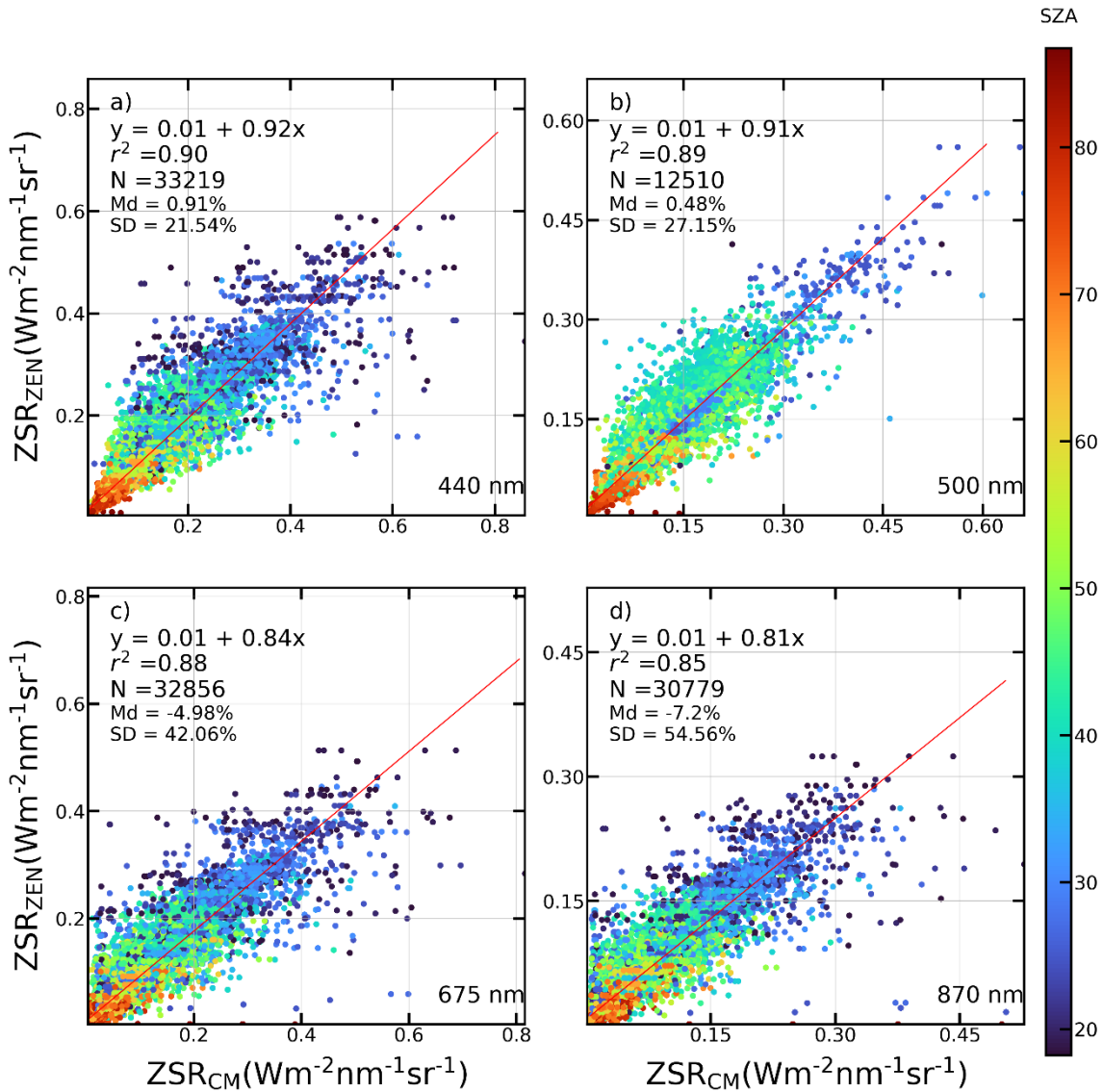


948



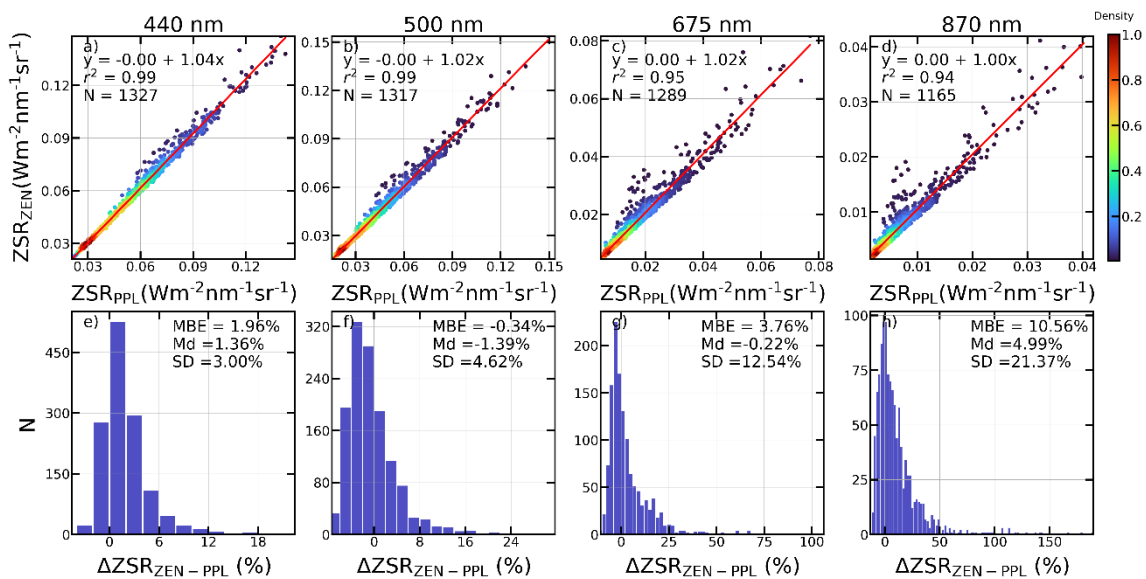
949
 950
 951
 952
 953

Figure 4. Density scatter plot of the zenith sky radiance simulated (ZSR_{SIM}) in radiance units against the ZEN-R52 measurements in arbitrary units (AU) corrected in dark signal and temperature (ZSR_{DSC_TC}) at a) 440nm, b) 500nm, c) 675 nm and d) 870 nm. Linear fit (red line) and its equation, determination coefficient (r^2) and number of data points (N) are also shown.



954
955
956
957
958

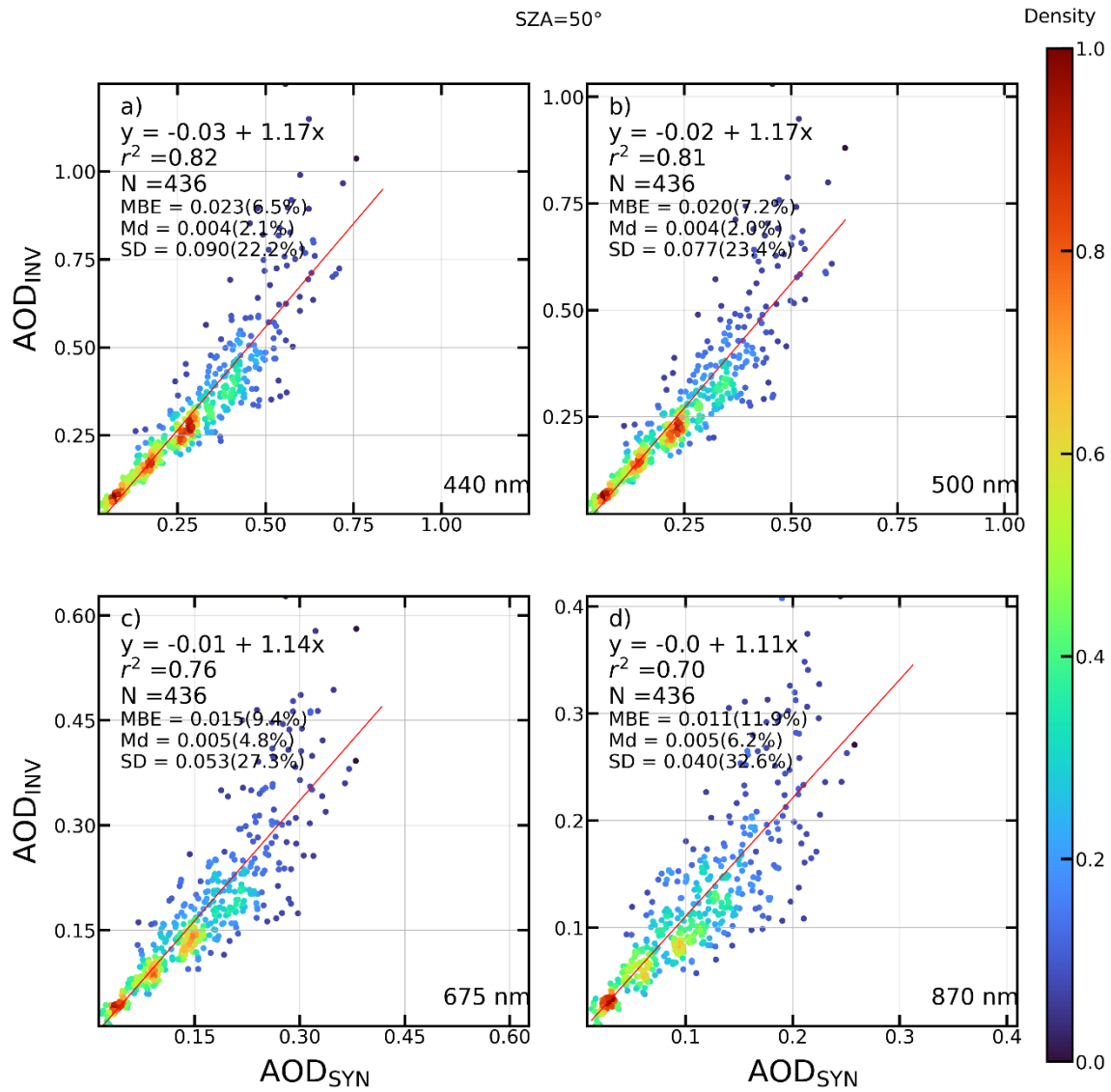
Figure 5. Scatter plot of the calibrated ZEN-R52 measurements (ZSR_{ZEN}) against coincident measurements from AERONET Cloud Mode (ZSR_{CM}) at a) 440nm, b) 500nm, c) 675 nm and d) 870 nm. Linear fit (red line) and its equation, determination coefficient (r^2) and number of data points (N) are shown. The median (Md) and standard deviation (SD) of the Δ differences are also shown. Points colours represent the SZA.



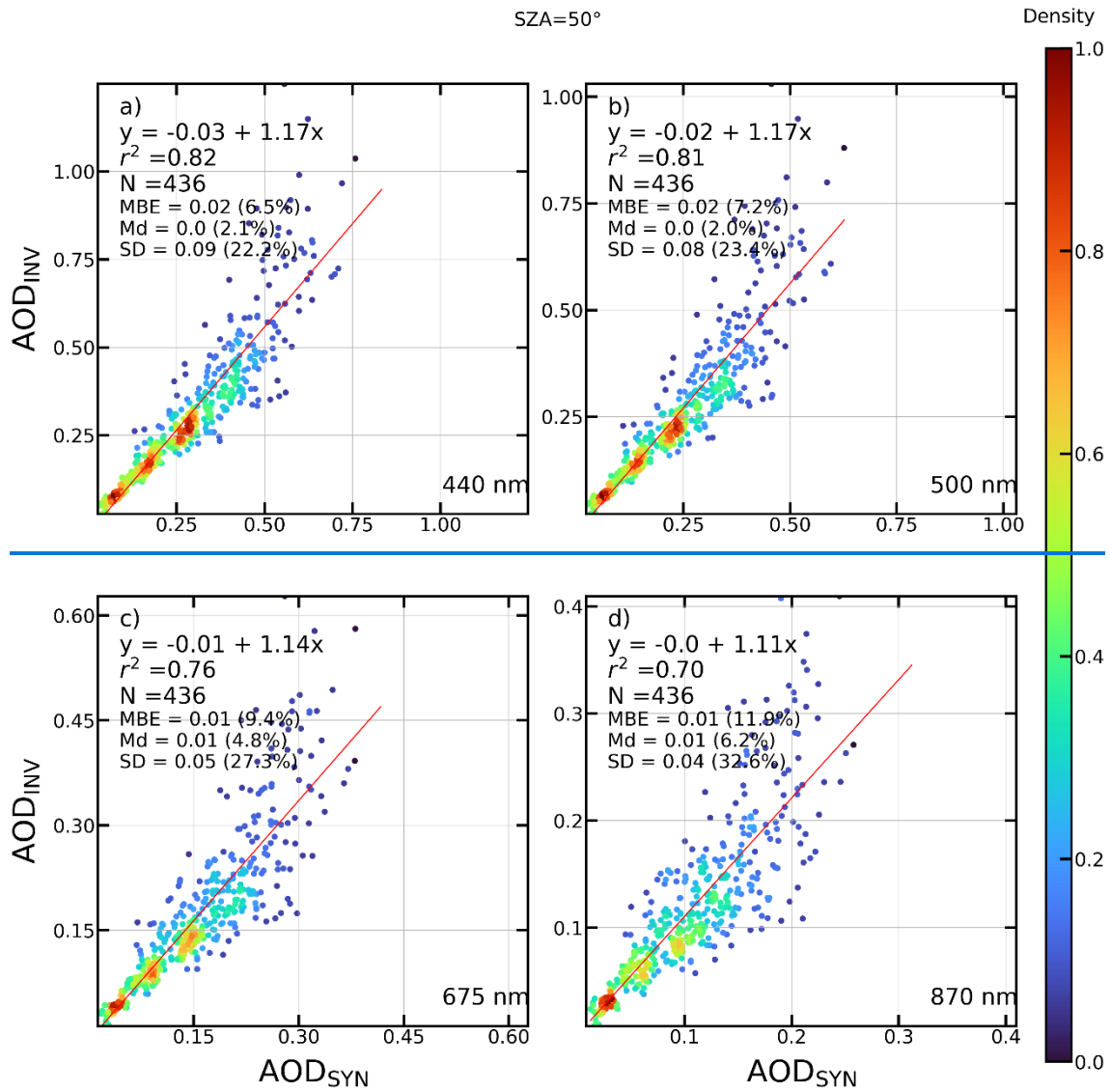
959

960
 961
 962
 963
 964
 965
 966
 967

Figure 6. (a-d) Density scatter plot of the calibrated ZEN-R52 measurements (ZSR_{ZEN}) against coincident zenith sky radiances derived from AERONET PPL measurements ($ZSR_{ZEN-PPL}$) at a) 440 nm, b) 500 nm, c) 675 nm and d) 870 nm. Linear fit (red line), its equation, determination coefficient (r^2) and number of data pairs (N) are shown. (e-h) Frequency histograms of the $\Delta ZSR_{ZEN-PPL}$ differences in AOD from ZEN-R52 and AERONET PPL e) 440 nm, f) 500 nm, g) 675 nm and h) 870 nm. The mean bias error (MBE), median (Md) and standard deviation (SD) of the differences are also shown.

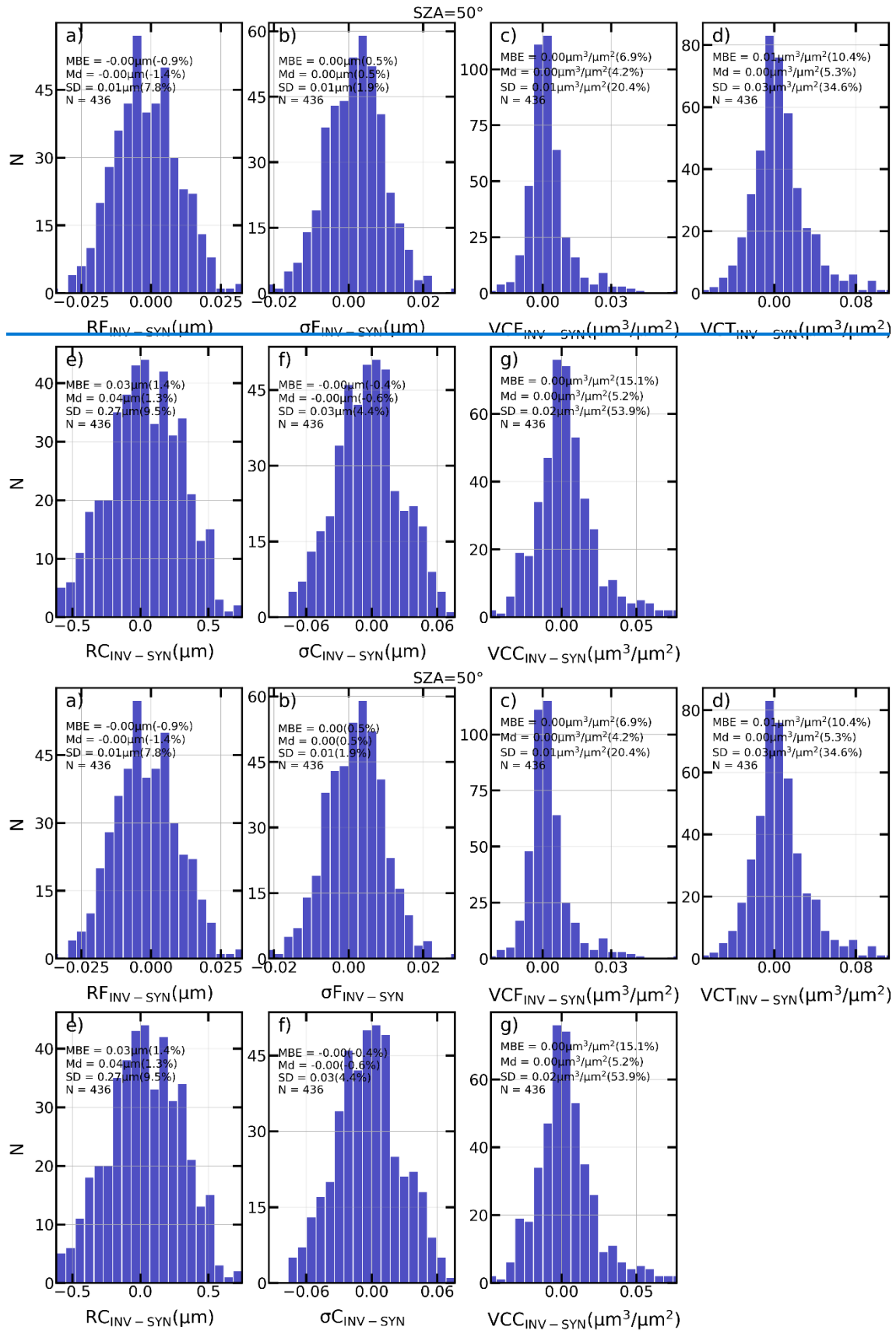


968



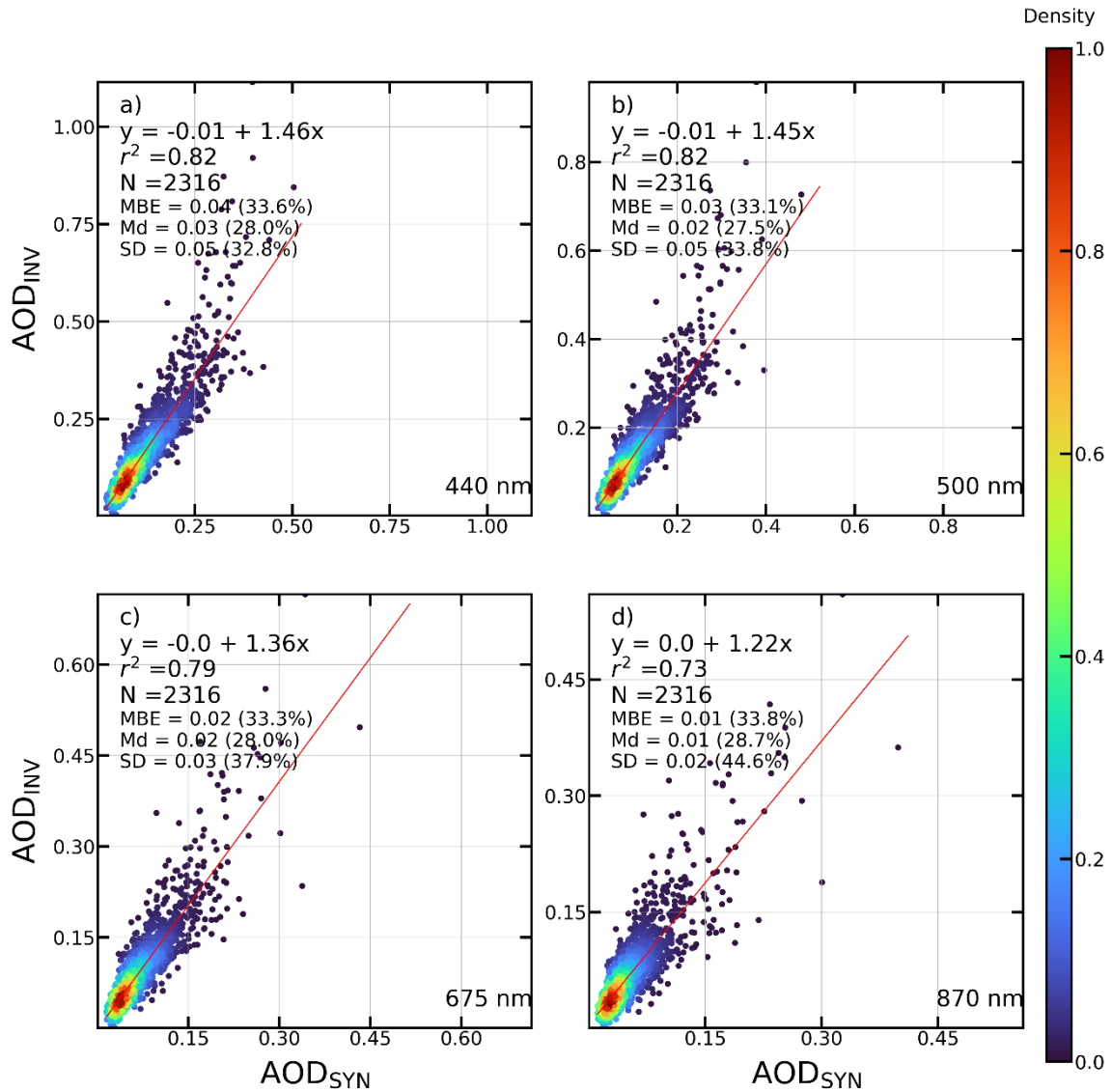
969
 970
 971
 972
 973
 974
 975

Figure 7. Density scatter plot of the AOD retrieved by GRASP after the inversion of synthetic ZSR (AOD_{INV}) against the initial AOD (AOD_{SYN}) obtained for synthetic scenarios created from the combination of five aerosol types for SZA=50° at a) 440nm, b) 500nm, c) 675 nm and d) 870 nm. Linear fit (red line) with its equation, determination coefficient (r^2) and number of data points (N) are shown. Mean bias error (MB), median (Md) and standard deviation (SD) of the absolute and Δ (between brackets) differences between the inverted and synthetic AOD are also included.



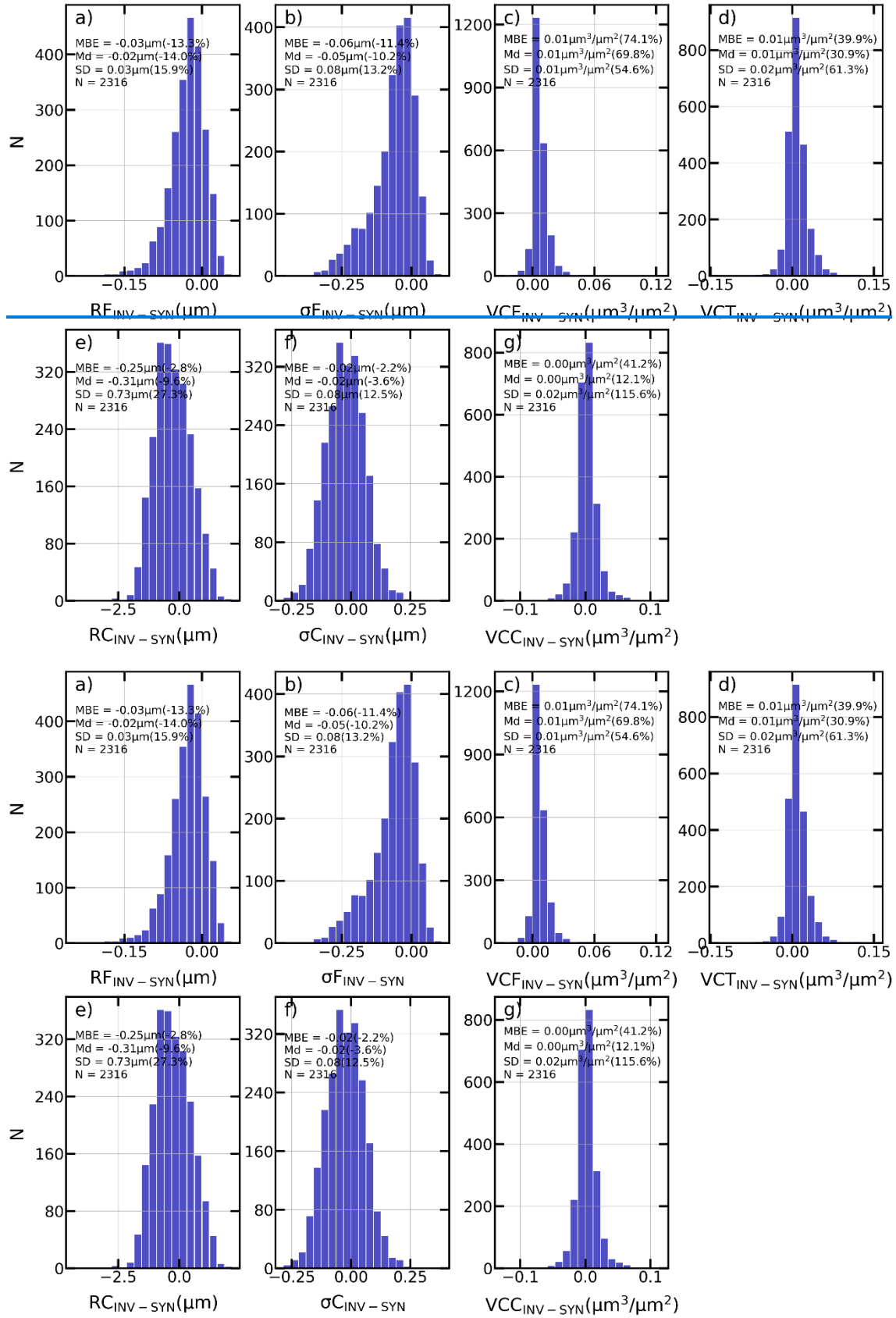
978 **Figure 8.** Frequency histograms of the absolute differences in the aerosol size distribution properties retrieved by GRASP after the inversion of synthetic ZSR (INV) and the ones initially obtained (SYN) for synthetic
 979 scenarios created from the combination of five aerosol types at SZA=50°. The mean bias error (MBE), median
 980 (Md) and standard deviation (SD) and their corresponding value for the Δ differences (between brackets) are
 981 also shown. These size distribution properties are volume median radius of fine (RF) and coarse (RC)
 982 modes,

983 standard deviation of log-normal distribution for fine (σ_F) and coarse modes (σ_C), and aerosol volume
 984 concentration for fine (VCF) and coarse (VCC) modes and the total (VCT).



985

986 **Figure 9.** Density scatter plot of the AOD retrieved by GRASP after the inversion of synthetic ZSR (AOD_{INV})
 987 against the initial AOD (AOD_{SYN}) obtained for synthetic scenarios created from AERONET retrievals at a)
 988 440nm, b) 500nm, c) 675 nm and d) 870 nm. Linear fit (red line) with its equation, determination coefficient (r^2)
 989 and number of data points (N) are shown. Mean bias error (MB), median (Md) and standard deviation (SD) of
 990 the absolute and Δ (between brackets) differences between the inverted and synthetic AOD are also included.



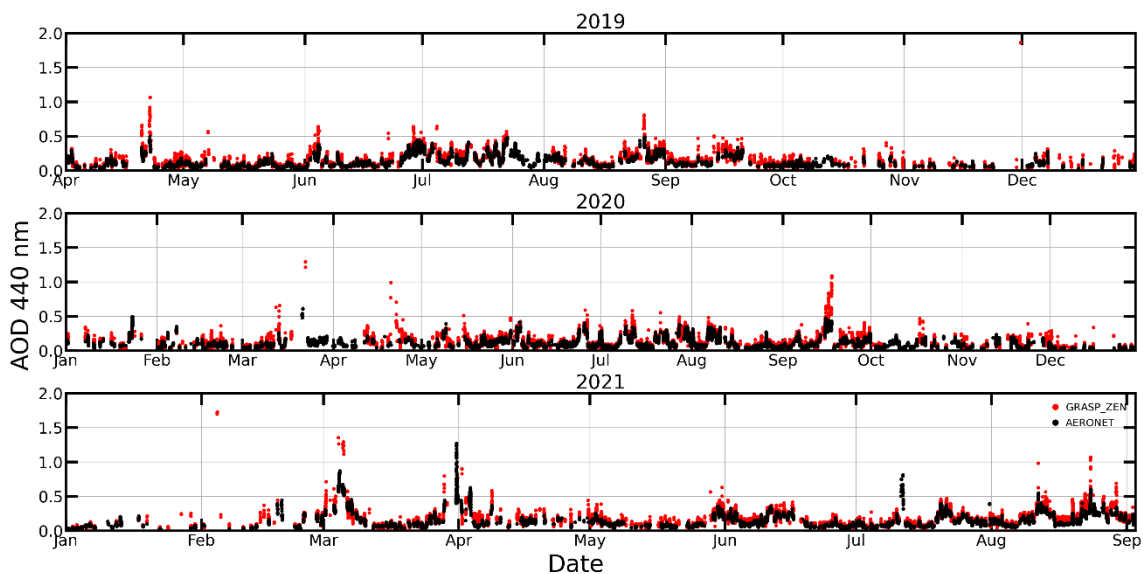
991

992

993 **Figure 10. Frequency histograms of the absolute differences in the aerosol size distribution properties retrieved**
 994 **by GRASP after the inversion of synthetic ZSR (INV) and the ones initially obtained (SYN) for synthetic**
 995 **scenarios created from AERONET retrievals. The mean bias error (MBE), median (Md) and standard deviation**
 996 **(SD) and their corresponding value for the Δ differences (between brackets) are also shown. These size**

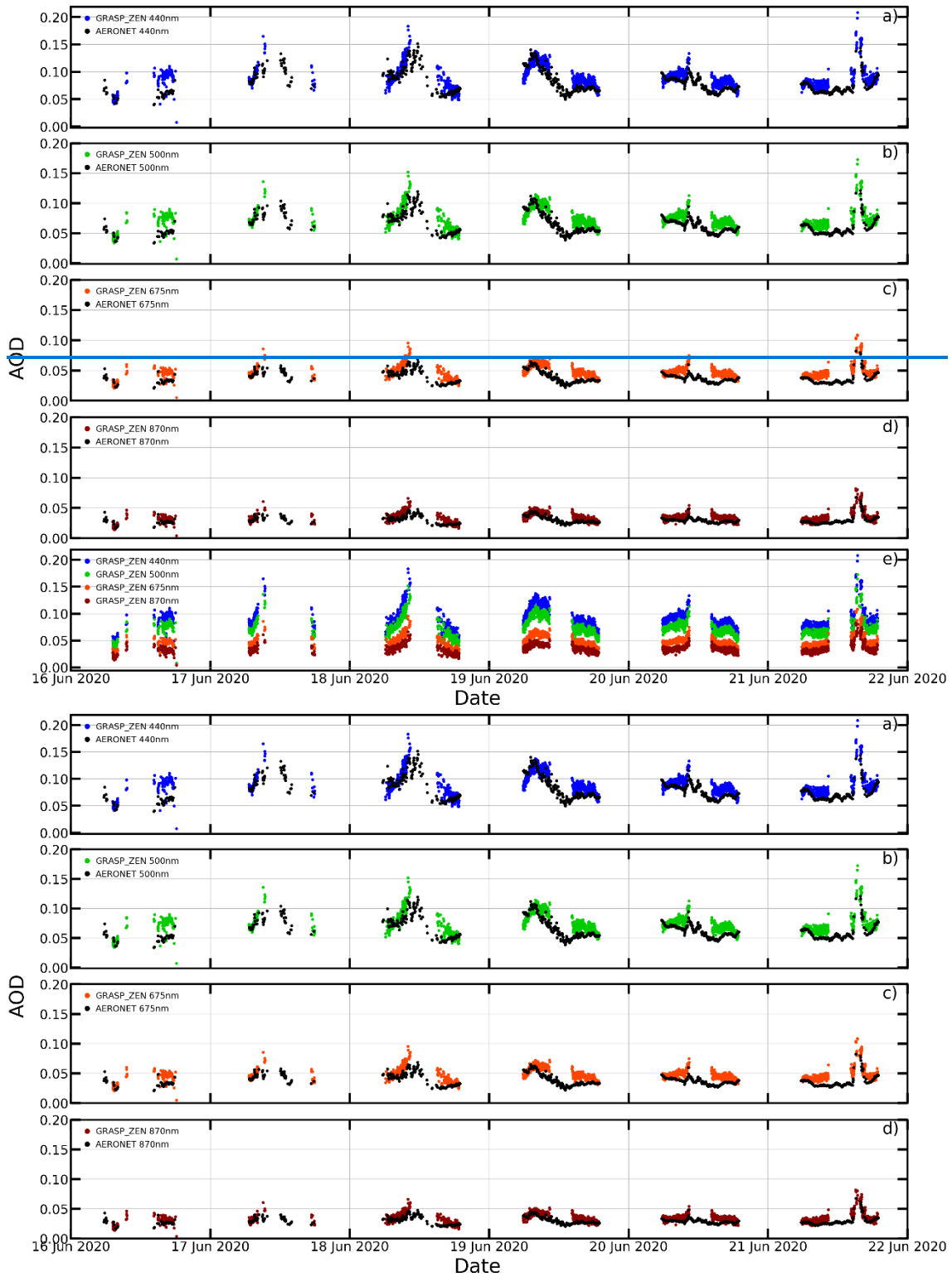
997 distribution properties are volume median radius of fine (RF) and coarse (RC) modes, standard deviation of
998 log-normal distribution for fine (σ_F) and coarse modes (σ_C), and aerosol volume concentration for fine (VCF)
999 and coarse (VCC) modes and the total (VCT).

1000



1001
1002
1003

Figure 11. Time series evolution of aerosol optical depth (AOD) at 440 nm retrieved by GRASP-ZEN and by AERONET at Valladolid for all the ZEN-R52 available dataset (April 2019 to September 2021).



1004

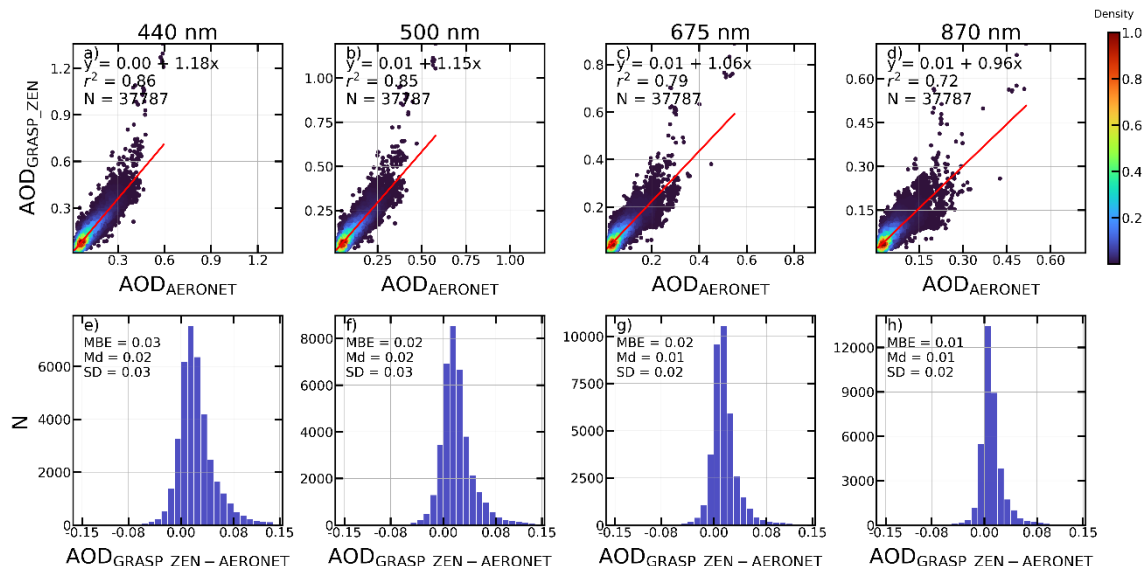
1005

1006

1007

1008

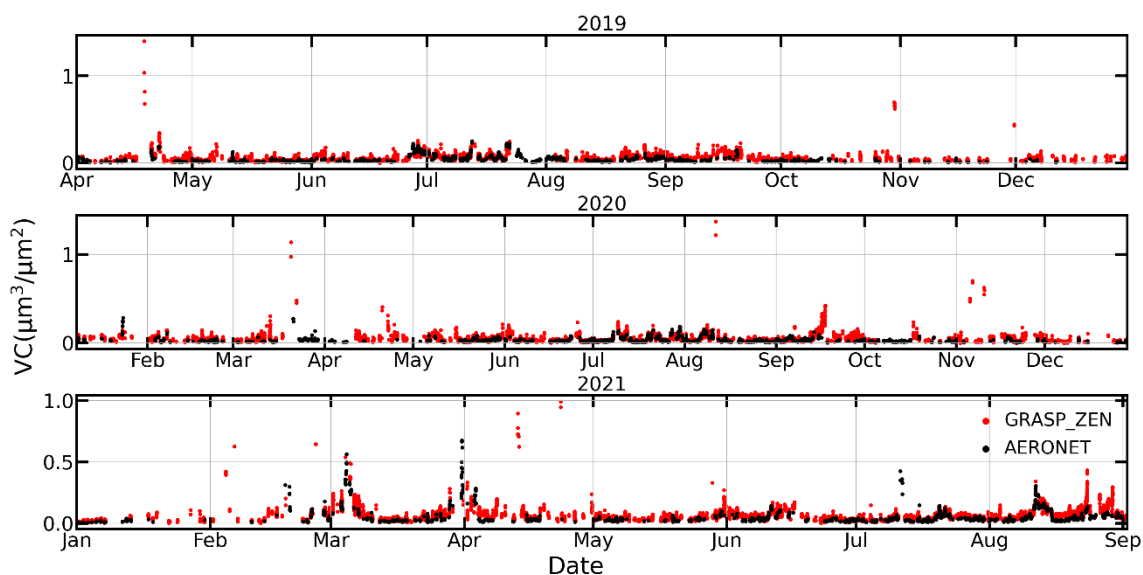
Figure 12. (a-d) Time series evolution of aerosol optical depth (AOD) at a) 440 nm, b) 500 nm, c) 675 nm and d) 870 nm retrieved by GRASP-ZEN and by AERONET at Valladolid for a week period in summer 2020 (16 to 22 June). (e) AOD retrieved by GRASP-ZEN for all ZEN-R52 channels plotted together.



1009

1010 **Figure 13. (a-d) Density scatter plots of the AOD retrieved by GRASP-ZEN (AOD_{GRASP_ZEN}) against coincident**
 1011 **measurement from AERONET (AOD_{AERONET}) at a) 440 nm, b) 500 nm, c) 675 nm and d) 870 nm. Linear fit (red**
 1012 **line), its equation, determination coefficient (r^2) and number of data pairs (N) are shown. (e-h) Frequency**
 1013 **histograms of the absolute differences in AOD from GRASP-ZEN and AERONET at e) 440nm, f) 500nm, g) 675**
 1014 **nm and h) 870 nm. The mean bias error (MBE), median (Md) and standard deviation (SD) are also shown.**

1015

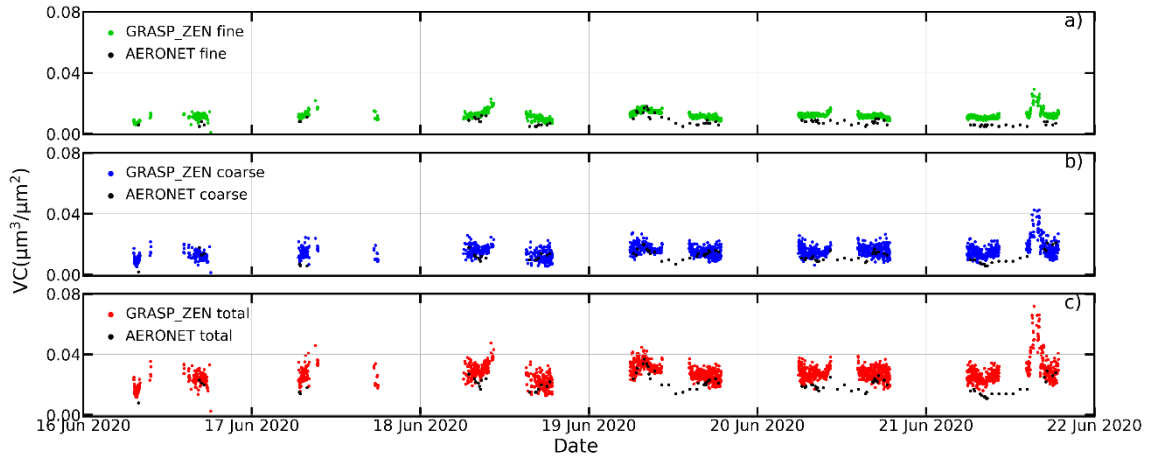


1016

1017

1018

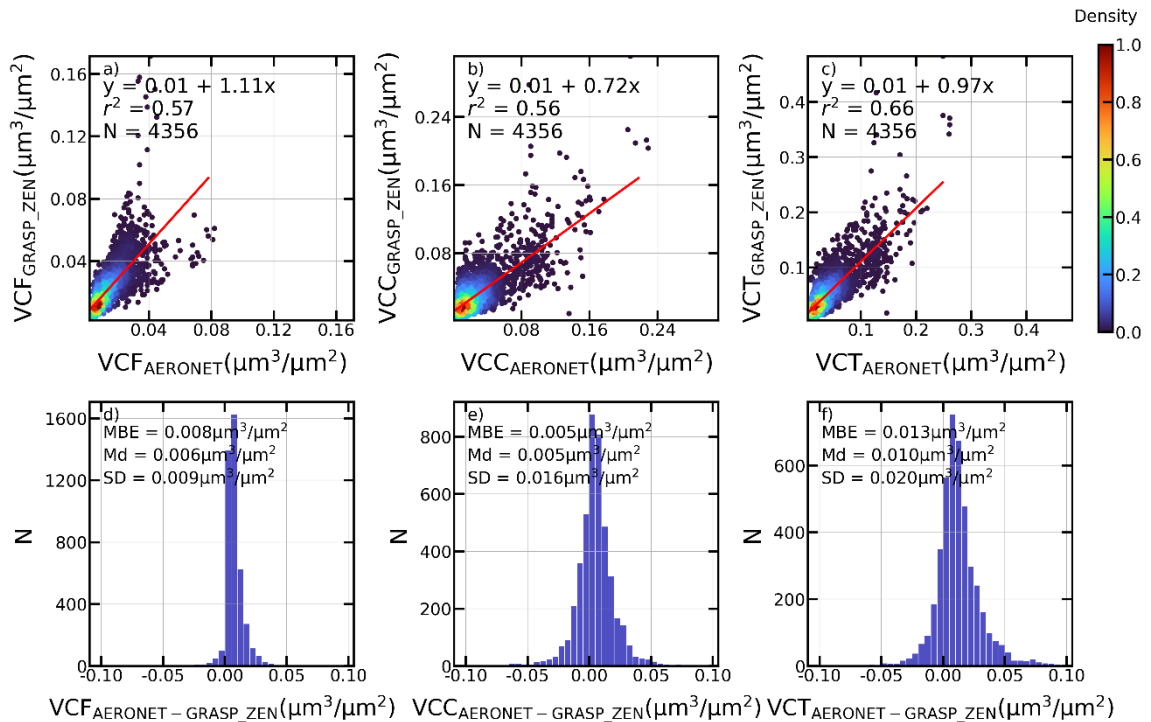
Figure 14. Time series evolution of the total volume concentration (VCT) retrieved by GRASP-ZEN and by
AERONET at Valladolid for all the ZEN-R52 available dataset (April 2019 to September 2021).



1019

1020 **Figure 15. Time series evolution of volume concentration for fine (VCF) and coarse (VCC) modes and the total (VCT) retrieved by GRASP-ZEN and by AERONET at Valladolid for a week period in summer 2020 (16 to 22**
 1021 **June).**

1023



1024

1025 **Figure 16. (a-c) Density scatter plot of the volume concentration for fine (VCF) and coarse (VCC) modes and**
 1026 **total (VCT) retrieved by GRASP-ZEN against coincident retrievals from AERONET. Linear fit (red line), its**
 1027 **equation, determination coefficient (r^2) and number of data points (N) are shown. (e-h) Frequency histograms**
 1028 **of the absolute differences between both datasets. The mean bias error (MBE), median (Md) and standard**
 1029 **deviation (SD) are also shown.**